# Space-time landslide susceptibility modelling in Taiwan

Zhice Fang[1,2], Yi Wang[1,*], Cees van Westen[2], Luigi Lombardo[2]

[1] Institute of Geophysics and Geomatics, China University of Geosciences, Wuhan 430074, China

[2] University of Twente, Faculty of Geo-Information Science and Earth Observation (ITC), PO Box 217, Enschede, AE 7500, Netherlands

[*]Correspondence Author: Yi Wang (cug.yi.wang@gmail.com)

## Abstract

Portraying spatiotemporal variations in landslide susceptibility patterns is crucial for landslide prevention and management. In this study, we implement a space-time modeling approach to predict the landslide susceptibility on a yearly basis across the main island of Taiwan, from 2004 to 2018. We use a Bayesian version of a binomial generalized additive model, which assumes that landslide occurrences follow a Bernoulli distribution. We generate 46,074 slope units to partition the island of Taiwan and divided the time domain into 14 annual units. The binary landslide label assigned to each slope unit and their temporal replicates come from an available landslide database, that contains an inventory for every year. We only consider new landslides or reactivations of previous mass movements in the yearly inventories. This information and its absence counterpart are regressed against a set of static and dynamic covariates.

Our modeling strategy features an initial explanatory model to test the goodness-of-fit and interpret the effect of covariates. Then, five cross-validation (CV) schemes are tested to provide a full spectrum of the predictive capacity of our model. Specifically, we implement a fully randomized 10-fold CV, a spatially constrained CV, two temporal

CV (a leave one year out and a sequential temporal aggregation), together with a spatio-temporal CV. We summarize the performance in each of these tests, through their pure numerical expression as well as their residual representation in space and time.

Overall, our space-time model produces excellent and interpretable results. We consider this type of dynamic prediction the new direction to take to finally move away from the static view provided by traditional susceptibility models. And, we consider such analyses just a stepping stone for further improvements, the most natural of which would lead to statistical simulations for future scenarios.

**Keywords:** landslide susceptibility; space-time modelling; slope unit; dynamic covariates

# 1. Introduction

Landslides are a widespread hazard typical of any mountainous landscape around the world, and they can represent a serious threat to human life and property (Rossi et al., 2019; Broeckx et al., 2020). Landslide susceptibility modelling is an important tool in the assessment of hazards and risks, because it provides the likelihood of where landslides may occur in a given area based on a set of environmental factors (Guzzetti et al., 2006; Van Westen et al., 2008; Reichenbach et al., 2018). Since its first conception though, a specific limitation has always affected the notion of landslide susceptibility. In fact, it is unanimously agreed that most susceptibility maps only related to the relative spatial likelihood of landslide occurrences, without indicating the temporal probability of occurrence, which is associated with the concept of hazard (Guzzetti et al., 1999). Also lacking is often an indication of how dangerous landslide may be, either in terms of its size (Lombardo et al., 2021), density, or in term of its impact pressure and runout characteristics (Corominas et al., 2014). This clear separation even explicitly appeared in international guidelines (Fell et al., 2008).

However, as variants such as near-real-time (e.g., Manconi and Giordan, 2016; Lombardo and Tanyas, 2020) or rainfall threshold (e.g., Monsieurs et al., 2019; Wang et al., 2021) models have demonstrated, probabilistic estimates of landslide occurrences can be also temporally obtained. Nevertheless, the original separation still implies that recent space-time susceptibility models (Wang et al., 2022) do not entirely fall within the definition of susceptibility because it explicitly excludes the temporal component, nor they solve the definition of hazard because it requires the inclusion of the size or energy associated with the moving mass. In this exact literature gap, we position this study, as it offers another example of how data-driven models can be extended far beyond what traditional susceptibility prescribes.

Before providing any further explanation on what space-time susceptibility models can do, it is important to stress that substantial improvements have been made since the early 1970s, when the concept of susceptibility was initially proposed (Reichenbach et al., 2018). Since then, the geoscientific community moved past subjective opinions on which slope may have been stable or not, either via field surveys or geomorphological mapping (e.g., Verstappen, 1983). The progress initially welcomed bivariate statistical models (e.g., Van Westen et al., 2003), and naturally evolved towards their multivariate counterparts mainly represented by generalized linear models (e.g., Atkinson and Massari, 1998). The multivariate context further differentiated over time, in the form of machine learning models (e.g., Marjanović et al., 2011) and their deep learning (Wang et al., 2019; Fang et al., 2021; Aguilera et al., 2022) extensions. In this plethora of available solutions, the way a potential user may navigate through them and understand their strength and weaknesses mainly depends on two elements. The first element corresponds to the interpretability and the second to the performance these methods can offer. These two extremes essentially direct the way data-driven models can be applied to the susceptibility context. Models that prioritize interpretation fall in the statistical category, whereas models that maximize performance belong to machine and deep learning ones. Between these two though, generalized additive models (GAMs) (e.g., Steger et al., 2016) offer enough flexibility to usually provide high performance while offering the same capacity to interpret the generated results, as in simpler statistical frameworks. Irrespective of what these models are best intended to do, they have in common their ability to be applied over large areas. In fact, in an ideal situation, one may want to model landslides respecting the law of physics that govern their instability process. However, the unavailability of required geotechnical parameters has traditionally confined the use of physics-based models (e.g., Montgomery and Dietrich, 1994) within relatively small regions (e.g., Van den Bout et al., 2021) where such information is still somewhat obtainable. Conversely, data-driven models can make use of proxy parameters. Nowadays, these can even be easily accessed through open repositories and cloud-based data management services (Titti et al., 2022a). Overall, landslide susceptibility based on data-driven models has been suitable for large areas, provided the availability of a sufficiently large landslide inventory. Even if its calibration is limited to a relatively small geographic area, the possibility to spatially transfer (extend in space) has always been there (Petschko et al., 2014), provided that the conditions area similar. An important scientific question is rather if and how the use of these models can be reliably extended in the temporal dimension. So far, most susceptibility models have been framed within the generally accepted assumption that the past is the key to the future (Guzzetti et al., 1999; Van Westen et al., 2008). This assumption has been recently challenged in the context of rainfall-induced landslides because global warming is now changing the spatio-temporal patterns of some predictors (e.g., Loche et al., 2022). Or, because the human intervention is actively modifying the slope equilibrium, either through land use changes (Hao et al., 2020) or road cuts (Tanyaş et al., 2022). Aside from these specific situations, as long as the effect of the trigger is suitably captured and fed to a data-driven model, it is theoretically possible to extend the otherwise traditionally stationary susceptibility framework towards a dynamic realization of the same, both in space and in time (Wang et al., 2022). Therefore, the temporal limitation in the susceptibility definition we mentioned above is not related to the available models, but to our capacity to capture the dynamic effects of predisposing and triggering factors.

A number of studies have actually started looking in this direction, with interesting examples on soil moisture (Gorsevski et al., 2006), land use/land cover (Meusburger and Alewell, 2009; Reichenbach et al., 2014; Chen et al., 2019b; Shu et al., 2019), and climatic variables (Hua et al., 2020; Scheidl et al., 2020; Fan et al., 2021). Samia *et al.* (2017) proposed that an appropriate susceptibility assessment for an area in Collazzone (Italy) may require the information of previous landslide occurrences as a predisposing factor. Within the same area, Lombardo *et al.* (2020a) extended this framework even further, by proposing the first Bayesian version of a poissonian space-time GAM applied in the context of landslide occurrences. However, the timespan the authors analyzed covered roughly a century. Thus, information on the precipitation trigger could not be directly conveyed to the model, simply because no reliable rainfall estimates were collected in the early period of the available multi-temporal inventory and because the landslide inventory lacks exact dates for many events. The model Lombardo *et al.* (2020a) proposed still potentially accounted for the missing rainfall regime by making use of covariates that acted at the latent level (Bakka et al., 2019). More recently, Wang et al. (2022) tested a frequentist version of a binomial GLM across the whole China for the time period between 1985 to 2015, producing susceptibility estimates based on static and dynamic covariates. Our contribution addresses the topic of space-time (or dynamic) susceptibility, which we opt to model chiefly by combining the strengths of the two articles mentioned above. Specifically, we present an implementation of a binomial GAM modeled in a Bayesian framework via the Integrated Nested Laplacian Approximation (INLA, Bakka et al., 2019). Also, we avoid the inclusion of latent covariates under the assumption that the variability in the spatio-temporal distribution of landslides can be captured by a combination of static and dynamic covariates.

We test this model in Taiwan, an island on the Pacific Ring of Fire, where earthquakes and tropical cyclones have been reported triggering a large number of landslides in the past several decades. A report on climate change in Taiwan indicates that the number of extreme rainfall days has increased (Tong et al., 2017), thus even more extensive landsliding events are expected in the coming future. In this context, our space-time susceptibility model can lay the foundations for a new dynamic prediction system. And, it is specifically because of its predictive task that we included a suite of cross-validation routines aimed at testing how efficiently landslides can be predicted in such a complex setting.

# 2. Study area

Our study area is the main island of Taiwan in the northwestern Pacific Ocean (**Fig. 1a**), with an area of 35,808 $km^2$. About 70% of the area is either hilly or mountainous (Chen et al., 2015). The plains are mainly concentrated on the west coast, where 90% of the population lives. Approximately 60% of Taiwan is covered by forest, of which natural forest, plantation forest, and bamboo account for 73%, 20, and 7%, respectively. The farmland and urbanized areas are mainly located in coastal plains and tablelands with elevation less than 800 m, accounting for 29% and 6.1% of the total land area, respectively (Chang et al., 2018).

The study area straddles over the Tropic of Cancer, and its climate is affected by the East Asian monsoon. The northern part of Taiwan has a humid subtropical climate, and most of the central and southern regions have a tropical monsoon climate. Due to its geographic location in the Pacific Ring of Fire and in the path of tropical cyclones, Taiwan frequently experiences earthquakes and typhoons, which may lead to disasters in the form of widespread landslides and debris flows. For example, the Chi-Chi earthquake ($M_w$ = 7.6) triggered more than 10,000 slope failures in 1999, with a total landslide area of more than 100 $km^2$ (Hung, 2000; Khazai and Sitar, 2004). Typhoon Morakot in August 2009 discharged an extremely large amount of rainfall causing 652 deaths and a total economic loss of approximately $ 3.3 billion. In this overall picture, more than 22,700 landslides were responsible for part of the losses, particularly in the south of Taiwan, where the total landslide area reached nearly 270 $km^2$ (Lin et al., 2011). This Typhoon also set a new rainfall record of 3059 mm measured at the Alishan station, far exceeding the previous record of 1987 mm set by Typhoon Herb in 1996 (Huang et al., 2017). Some Typhoons with a similar path to Morakot also generated numerous landslides in southern Taiwan. For example, Typhoons Mindulle, Haitang, and Kalmaegi brought 399, 1632, 312 new landslides in the Kaoping watershed, respectively (Chen et al., 2013). Typhoon Aere in 2004 can be viewed as the worst event striking northern Taiwan in recent years, triggering 421 landslides in the Baichi watershed (Chiang and Chang, 2009).

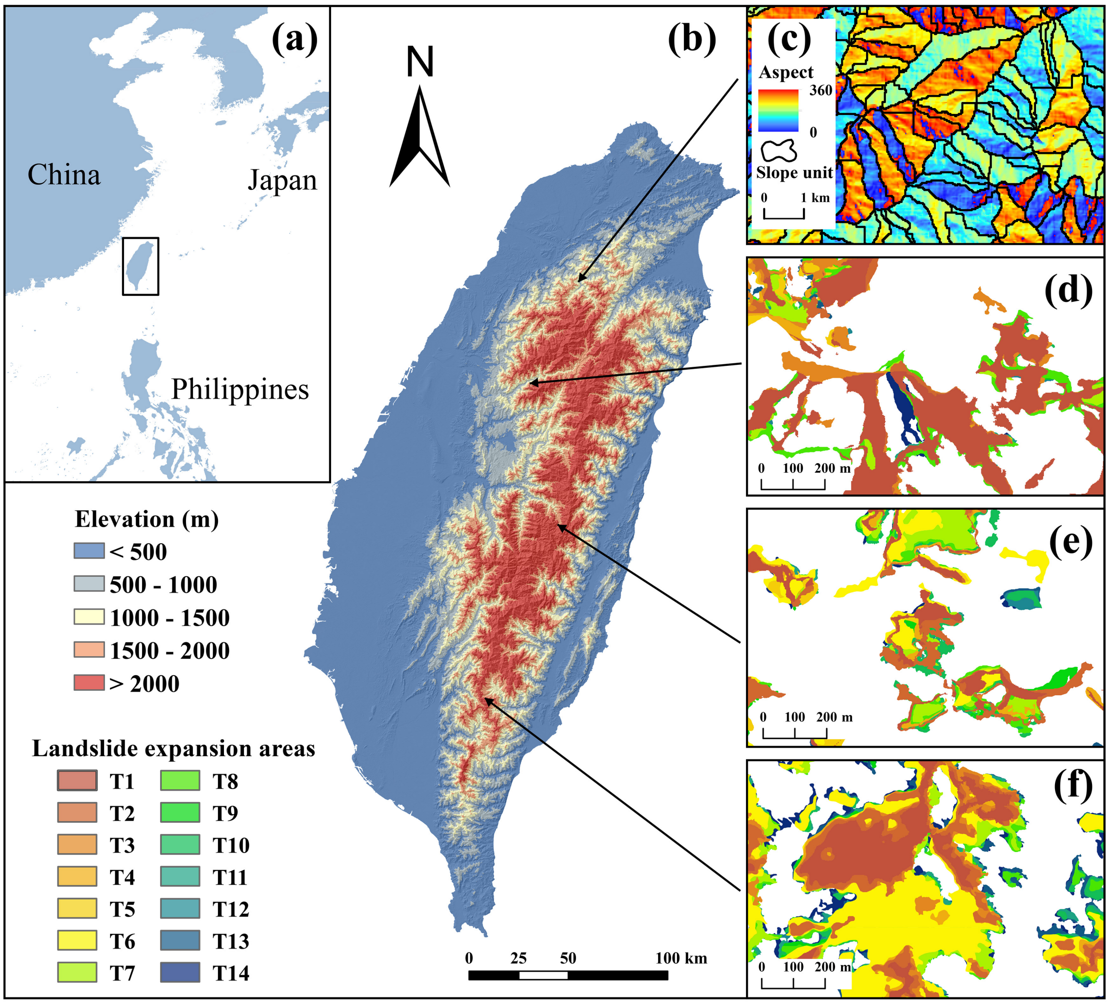


**Fig. 1** (a) Location of the study area; (b) elevation distribution of Taiwan island; (c) a sub-region showing the slope units partition, and (d-f) spatial distribution of landslides in four sub-regions from 2004 to 2018. Landslides in each time period denotes the expansion area from August 1st of the current year to August 1st of the next year.

# 3. Material and methods

## 3.1. Mapping and temporal units

Our model requires the selection of appropriate units to partition the terrain. With regards to the spatial dimension, the geoscientific community usually refers to mapping units in which the geographic space is divided. Specifically, in the context of data-driven models for landslide prediction, four main types of automatically generated mapping units can be found in the literature namely, geomorphological units (Meijerink, 1988; Seijmonsbergen, 2013), unique condition units (UCU; Calcaterra et al., 2010; Titti et al., 2021), slope units (SU; Carrara, 1983; Carrara et al., 1991) and grid-cells (GC; Fang et al., 2020; Lima et al., 2021). GC units are most frequently used in landslide susceptibility studies, and the SU delineation coming second (Reichenbach et al., 2018). However, SU have seen a great progress in recent years thanks to the creation of open tools capable of automating the SU delineation procedure (Alvioli et al., 2016). Their strength resides in the capacity of mimicking realistic geomorphological features – a landscape is not divided into GCs but rather into slopes –, and the fact that they reflect a scale at which geotechnical solutions can take place – when a stabilization project takes place one does not stabilize a single GC or even a cluster of GCs, but one rather stabilizes a slope. In addition to these characteristics, SUs partition the landscape into a much smaller number of objects compared to the GC case. In turn, the computational burden is smaller, making SU an ideal mapping unit for modelling large spatio-temporal domains such as Taiwan and 15-years of landslide records.

We recall here that our study focuses on the whole main island of Taiwan, which contains large flat areas (e.g. plains, tablelands). These can be considered as trivial areas (Steger et al., 2021b), and excluded from the analysis in the first place as no landslide can take place there.

Therefore, we excluded these flat areas from the SU partition. Also, flat SUs where the aspect often produces Not-A-Number values should always be eliminated to avoid any artifact in the resulting polygons (Alvioli et al., 2020). To numerically recognize flat areas, we first used the r.geomorphon module (Jasiewicz and Stepinski, 2013) in GRASS GIS. These were then passed to the r.slopeunits software proposed by Alvioli *et al*. (2016), which focuses on the automatic SU delineation on the rough topography of Taiwan (27,176 km$^2$). As a result of parameterization tests we initially ran (not reported here), we obtained a r.slopeunits configuration with a minimum SU area of 150,000 $m^2$ and a circular variance set at 0.6. The resulting SU partition produced 46,074 polygons with a mean slope unit area of 589,844 $m^2$ and an associated variability of 395,973 $m^2$ measured in a single standard deviation.

Regarding the temporal dimension, the choice of the temporal unit was quite straightforward as the available landslide inventory was mapped on a yearly basis. Therefore, we opted for a temporal unit of one year, for a total of 14 years under consideration. Overall, partitioning our space-time domain produced 645,036 units (46,074 SU multiplied by 14 temporal units).

## 3.2. Landslide data

Typhoon Morakot hit Taiwan in August 2009, causing numerous landslides which prompted concerns with the local administration on how to manage this geohazard. As a result, the Forestry Bureau of Taiwan commissioned the National Cheng Kung University to produce a multi-temporal landslide inventory across the island, on a yearly basis. The geomorphological mapping covered the 2004-2018 period. The expert landslide and shaded area delineation system (ELSADS) was used to produce each landslide inventory maps (Lin et al., 2013). The Formosat-2 satellite images (2 m spatial resolution) from January to July each year were selected for landslide interpretation. The final recognition results were verified by visual interpretation of aerial images with a spatial resolution of 25 cm, and the overall accuracy reached 98%, details refer to Lin et al. (2013).

However, the landslides are not filtered with respect to the previous years. In other words, if a landslide is present in one year it will also be present in the next year, if it is still interpretable in the images. Differences can be brought due to revegetation, which may obscure part or the whole landslide signature on the optical images. Or, if the landslides have been re-activated or re-mobilized, the previous surface can be expanded. Because of this, we opted to take the difference between two subsequent landslide maps. As a result, we can recognize landslide expansions, apparent shrinking (revegetated) landslides and entirely new failures. For instance, if we calculate the landslides for the year 2005 minus those of 2004, then positive values imply new failed surfaces whereas negative values imply new vegetation growing on a landslide scar. It is also important to stress that the time period used for mapping does not cover a traditional year (January 1st to the next), but time period used extends from the first of August to the last day of July of the next year. Each of these time periods is described in Appendix A. This is due to the fact that the quality of satellite imagery (cloud-cover-wise) is at its best from January to July of each year.

As a result of the iterative yearly difference of the available maps, we obtained 14 new landslide maps, from the 1st August 2004 to the 31st July 2018. From each of these we had excluded the landslide areas that underwent revegetation, and made the choice to focus on new failures and revegetated landslides (**Fig. 1**). This does not imply that we assumed revegetated areas to be stable. We simply chose to focus on landslide initiation processes and build a model capable of predicting new ones. In order to avoid that very small failure rendered the slope unit as "unstable", we opted to include a minimum landslide surface area threshold of 1000 $m^2$. Slope units with a landslide area greater than 1000 $m^2$ were assigned with a presence status (1), while the remaining slope units were labeled with a landslide absence status (0). We set this threshold because the minimum size of mapped landslides is actually 1000 $m^2$, as described in Lin et al. (2013) and Chen et al. (2019c).

## 3.3. Covariates

All landscape, environmental, tectonic and climatic characteristics change with time, but in the considered temporal domain of 14 years, some covariates may vary much faster than others. In turn, this implies that a space-time susceptibility can make use of temporally-stationary covariates, which have mostly geological and morphometrical origins. Furthermore, it can integrate dynamic ones such as vegetation cover, ground motion and rainfall patterns. **Table 1** presents the preliminary set of covariates we opted in this study, including 11 static covariates and 7 dynamic ones. Specifically, we downloaded the new version of the 30m SRTM DEM (accessible at https://earthdata.nasa.gov/) and calculated five terrain derivatives : slope (Zevenbergen and Thorne, 1987), plan and profile curvatures (Heerdegen and Beran, 1982), eastness and northness (Lombardo and Mai, 2018). These covariates are quite common in the landslide susceptibility literature and constitute the bulk of most of the articles on this topic (Reichenbach et al., 2018). To them, we also added the lithology, expressed into 26 classes reported in the 1:500,000 geological map (http://gis.geo.ncu.edu.tw/) compiled in 1999, provided by the Graduate Institute of Applied Geology, National Central University (see Appendix B for the legend). The above-mentioned topographic and lithologic covariates represent the group of stationary covariates in our space-time model.

As for the non-stationary covariates, we considered earthquake-, rainfall- and vegetation- related factors, due to the location of Taiwan along the western circum-Pacific seismic belt and in the path of tropical cyclones.

For the seismic covariates, we collected all the available peak ground acceleration (PGA) data for Taiwan from the USGS ShakeMap system (Worden and Wald, 2016), from 2004 to 2018. We recall here that the ShakeMap system only reports ground motion data for earthquakes with magnitudes greater than 5.0. From all these events, we then calculated the maximum and cumulative PGA values for each year, under the assumption that successive earthquakes larger than a certain threshold may also contribute to slope failures. Tanyaş and Lombardo (2019) reported that 90% of the landslides from the available co-seismic inventories in a USGS database, falls within a 0.12 g PGA contour value. Therefore, in addition to the two ground motion parameters (max and sum) mentioned above, we also included a covariate expressing the number of times per year that the PGA in a given location exceeded 0.12 g.

For representing the effect of precipitation, Chen *et al*. (2013) and Chen *et al*. (2015) pointed out that the hourly maximum within 24 hour is the most effective predictor of landslide occurrence in Taiwan. However, hourly rainfall data are difficult to obtain, especially for long periods, and they are not consistently available for all rain stations in Taiwan. Therefore, we compromised by using the maximum of all daily rainfall records within a year, for every year under consideration. Specifically, we collected daily rainfall data from 188 meteorological stations, computed the maximum rainfall and then interpolated the yearly patterns via cokriging, including the elevation (Diodato, 2005), to account for the orographic control on rainfall patterns (Goovaerts, 2000).

For representing the potential effect of vegetation, we used the normalized difference vegetation index (NDVI). Through Google Earth Engine, we extracted the maximum NDVI values for each time period based on Landsat 7 images. The selection of the annual maximum NDVI has two positive implications. The first is that it has already been used in the context of landslide applications providing good results (Yang et al., 2019; Saito et al., 2022). The second reason is that the maximum values best corrects for NDVI gaps (missing-data) caused by the scan line corrector failure of Landsat-7.

After extracting the annual maximum NDVI, we opted to further re-classify it into three classes: < 0, 0–0.5, and > 0.5. This operation ensures that we can specifically focus on portions of the NDVI distribution with a clear interpretation. For instance, negative NDVI values imply bare lands, then 0 < NDVI < 0.5 indicates sparsely vegetated regions and NDVI > 0.5 indicates forested area. To make use of these classes in the context of the mapping units, we then calculated their respective percentages per SU.

We recall here that the yearly expression of each dynamic covariate is generated from each 1st August to the next.

**Table 1** Summary of initial covariates used in the study.

| Type | Covariates | Description |
|---|---|---|
| Static | Mean slope<br>Standard deviation of slope<br>Mean plan curvature<br>Standard deviation of plan curvature<br>Mean profile curvature<br>Standard deviation of profile curvature<br>Mean northness<br>Standard deviation of northness<br>Mean eastness<br>Standard deviation of eastness | Mean and standard deviation of morphological factors in each slope unit. |
| | Lithology | Majority class in each slope unit. |
| Dynamic | Maximum daily rainfall | Mean of maximum daily rainfall per year in each slope unit. |
| | Percentages of NDVI class 1 | Proportion of NDVI less than 0 per year in each slope unit. |
| | Percentages of NDVI class 2 | Proportion of NDVI between 0 and 0.5 per year in each slope unit. |
| | Percentages of NDVI class 3 | Proportion of NDVI above 0.5 per year in each slope unit. |
| | Maximum PGA | Mean of maximum PGA per year in each slope unit. |
| | Accumulative PGA | Mean of accumulative PGA per year in each slope unit. |
| | Impact times of earthquakes | Mean of impact times per year in each slope unit. |

## 3.4. Generalized additive model

A generalized additive model (GAM) can integrate linear (or fixed) and nonlinear (or random) effects (Goetz et al., 2011; Lombardo et al., 2020b). Thus, this framework is able to produce flexible models usually characterized by high performance and straightforward interpretation (Lima et al., 2021)..

In the context of landslide susceptibility, the main modeling task is to distinguish locations that are stable from the unstable ones (or landslide absences from presences). In a GAM, this can be achieved by assuming that the two labels mentioned above follow a Bernoulli distribution. Because of the traditional susceptibility definition, the aforementioned assumption is meant over the geographic space. As we use a space-time model, we extend the binomial distribution assumption in both dimensions: space (slope units) and time (yearly periods).

Moreover, as we are interested in exploring model uncertainties, we opted for a Bayesian version of a binomial GAM, which we implemented via the R-INLA package (Rue et al., 2009). As a result, the generic formulation of our binomial GAM can be denoted as follows:

$$\eta(P) = \beta_0 + \sum_{i=1}^{n} \beta_i x_i + \sum_{j=1}^{m} f_j(x_j) + f(litho) \qquad (1)$$

where $\eta$ is the logit link, $P$ is the landslide susceptibility, $\beta_0$ is the global intercept, $\beta_i$ are the regression coefficients associated with a number of covariate $x_i$ used linearly, $f_j$ are the functions or collections of regression coefficients estimated by using a random walk of the first order (*rw1*) for a number $j$ of covariates $x$ used nonlinearly (Krainski et al., 2018). We recall here for simplicity that a *rw1* constrains the regression coefficients to be sequentially dependent. In other words, each class of a given nonlinear covariate is assigned with a regression coefficient which is estimated as a function of the regression coefficient of the adjacent classes. This procedure retains the ordinal structure of the original numerical properties before reclassification, and it is very different from what happens in the case of pure categorical properties. The latter is modeled by obtaining a regression coefficient per class which is independent to any other class in a given covariate. Such type of modeling structure is commonly referred to as independent and identically distributed (*iid*). In our case, we only used the outcropping lithology in Taiwan in such a way and the term $f(litho)$ in Eq. (1) represents the *iid* effect estimated for the lithology. We stress here that we do not mention any specifics in this section because the actual choice of which variable to use linearly or nonlinearly comes from a variable selection procedure that we will briefly illustrate later at the beginning of the Section 4.

## 3.5. Model validation

We evaluated the model performance from two aspects, its goodness-of-fit and its predictive performance. In both cases, we used the receiver operating characteristic (ROC) curve and area under the curve (AUC) to quantify the performance (Bradley, 1997). First, the model was fitted using 100% of the dataset to assess the goodness-of-fit and interpret the effects of the covariates. As regards the predictive performance, we explored it via five different cross-validation schemes, which are listed below:

(1) Purely random 10-fold cross-validation (*10fold-CV*): This procedure randomly splits the original dataset into 10 mutually exclusive and equal-sized subsets. Each subset contains 10% of the slope units in the whole space-time domain. The model is fitted using nine subsets, and the performance is measured in predicting the subset that has been left out. The above process is then repeated ten times for each subset.

(2) Spatial leave-one-out cross-validation (*S-CV*): This validation procedure generates 10 spatial subsets by dividing the entire study area into 10 sub-regions. Each subset contains slope units for all time periods with a specific spatial sub-region. We leave out one of the ten spatial subsets for validation and fit the model using the remaining nine subsets. The procedure is repeated 10 times by leaving out the subset of each sub-region.

(3) Temporal leave-one-out cross-validation (*T-CV*): This validation scheme is similar to the S-CV, the difference being the removal of one year at a time.

Specifically, we calibrate using 13 temporal subsets and validate on the complementary one. This procedure is repeated 14 times, for each year from 2004 to 2018.

(4) Temporal forward validation (*TF-CV*): This validation scheme sequentially tests the capacity of the susceptibility in predicting each period on the basis of the previous years. In other words, the first step essentially calibrates on T1 and validate on T2. Then, the following test calibrates on T1 and T2 combined, and validates on T3. This process is sequentially repeated until the data of T14 is validated on a calibrated model that combines all years from T1 to T13.

(5) Spatio-temporal leave-one-out cross-validation (*ST-CV*): This validation scheme divides the dataset into 140 subsets based on the combination of the 10 spatial sub-regions used in the S-CV and 14 time periods used in the T-CV. It boils down to calibrating over 139 subsets and validating on the excluded one, repeating the procedure 140 times.

# 4. Results

## 4.1. Model construction and goodness-of-fit

In the modelling process, we first determined the most appropriate way to use the covariates that we initially considered and which one we should actually introduce into the model. Specifically, these procedures respectively imply the choice on whether to use the given variable linearly or not and whether the given variable is useful to the model.

To address the first question, we implemented a series of pre-processing tests where each explanatory variable was separately tested in a univariate binomial GAM as a nonlinear property. If the estimated effect of the given variable against the landslide presence/absence resulted in a clear nonlinear relation, we then noted this characteristic down. In the second stage, we used a forward-stepwise procedure to estimate whether the inclusion of each variable (in their linear or nonlinear fashion checked before) would introduce relevant information (i.e., we kept it) or whether the information was redundant (i.e., we removed it). The forward-stepwise selection relied on the deviance information criterion (DIC) (Spiegelhalter et al., 2002), with a lower DIC value being an indicator of a better suite of variables or of a better model in general.

In practice, the way we implemented the stepwise procedure was to initially run all single-variable models, then picking the one with the lowest DIC and then move to select the best two-variable model, then triple and so on, up to the point where the DIC did not decrease any further (below an improvement threshold of 100) as we added new information. An overview of this procedure is provided in **Table 2**. There, one can notice the best model to include SlopeSD, ProfileSD, EastSD, and NorthSD among the linear covariates and SlopeM, NDVI3, Lithology, RainMax, PlanM, EastM, NorthM, and ProfileM among the non-linear ones (See **Table 1**, further details on their interpretation are provided in Section 4.2).

This combination constitutes the structure of our explanatory space-time model, and its goodness of fit is shown in **Fig. 2,** via the ROC curve and its integral. The resulting AUC is 0.845, which corresponds to an excellent classification according to Hosmer and Lemeshow (2000).

**Table 2** results of the forward-stepwise covariate selection

| Step | Selected covariate | DIC | Improvement threshold |
|---|---|---|---|
| 1 | SlopeM | 583,469 | / |
| 2 | NDVI3 | 541,419 | 42,050 |
| 3 | Lithology | 517,140 | 24,279 |
| 4 | RainMax | 512,189 | 4951 |
| 5 | PlanM | 507,525 | 4664 |
| 6 | EastM | 503,076 | 4449 |
| 7 | NorthM | 498,586 | 4490 |
| 8 | ProfileM | 496,837 | 1749 |
| 9 | SlopeSD | 495,747 | 1090 |
| 10 | ProfileSD | 495,320 | 427 |
| 11 | EastSD | 495,035 | 285 |
| 12 | NorthSD | 494,515 | 520 |
| 13 | PGAmax | 494,472 | 43 |

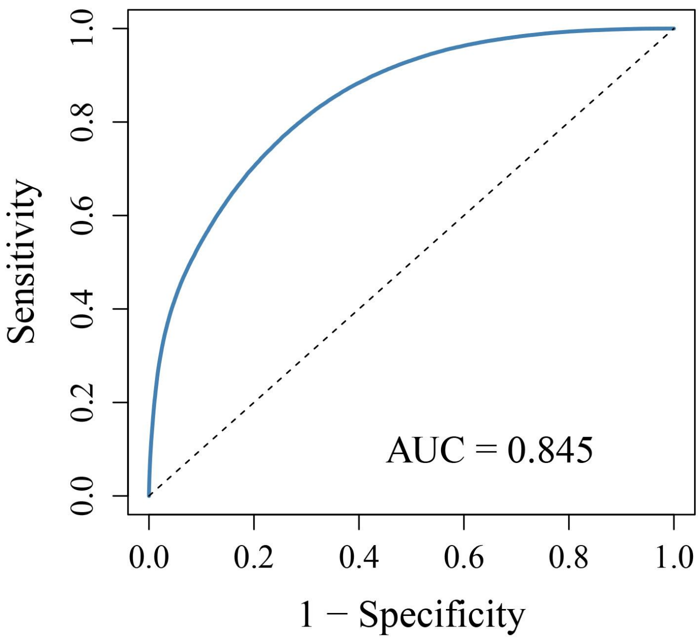


**Fig. 2** Goodness-of-fit of the model.

## 4.2. Covariate's effects

The linear or nonlinear model components are shown in **Fig. 3**. We recall here that being our binomial GAM Bayesian in nature, each covariate effect was estimated with a complete distribution, which was summarized via its mean value and its 95% width of the credible interval.

To clarify how to interpret these plots, for the linear and *iid* cases, we consider it significant for any covariate whose regression coefficient distribution does not contain zero, or better any covariate whose 2.5 and 97.5 percentiles share the same sign. As for the nonlinear case, we consider non-significant for any covariate whose effect contains zero throughout the whole depicted function. Non-significance does not necessarily mean that the given variable does not contribute to the whole model (this can be generally estimated through the absolute mean value), it merely informs that the model is uncertain, with a 95% confidence of its role in the model.

Inspecting **Fig. 3**, one can see that SlopeSD is associated with a mean negative regression coefficient, whereas the ProfileSD, NorthSD, and EastSD play an opposite role. Slope steepness with narrow credible intervals positively influences the landslide occurrences from 22º to 70º. Plan curvature and profile curvature have strong nonlinear effects. The plan curvature shows a positive effect between -0.15 and 0.18, and the profile curvature maintains a positive effect up to 0.1. We decomposed the topographical aspect into northness and eastness to conveniently illustrate the cyclic effect on landslides. The nonlinear effects of northness and eastness show that slope units facing south and east have a higher correlation with landslide occurrences.

Rainfall is a very important factor that controls landslide occurrences, especially in the Taiwan region with frequent typhoon events. In **Fig. 3,** we observe that the maximum daily rainfall has a significant effect with narrow credible intervals, and shows a positive effect with rainfall above 740 mm per day. As for the NDVI covariate, the class 3 (forested areas) achieves narrow credible intervals with the percentage above 80, showing a negative effect on landsliding. We recall here that the reclassification of the continuous NDVI into three categories is to eliminate the influence of pre-existed landslide scars. For the lithology covariate with the *iid* form, 22 classes shows significant effects on landslide occurrences. Specifically, the class B (Pleistocene andesite) has the highest negative effect, and the class P (Pliocene to Pleistocene mudstone and allochthon), O (Pliocene sandstone, mudstone, and shale), and U (Late Miocene to Pliocene shale, siltstone, sandstone) are three positive lithology categories that achieves the regression coefficients above 1.

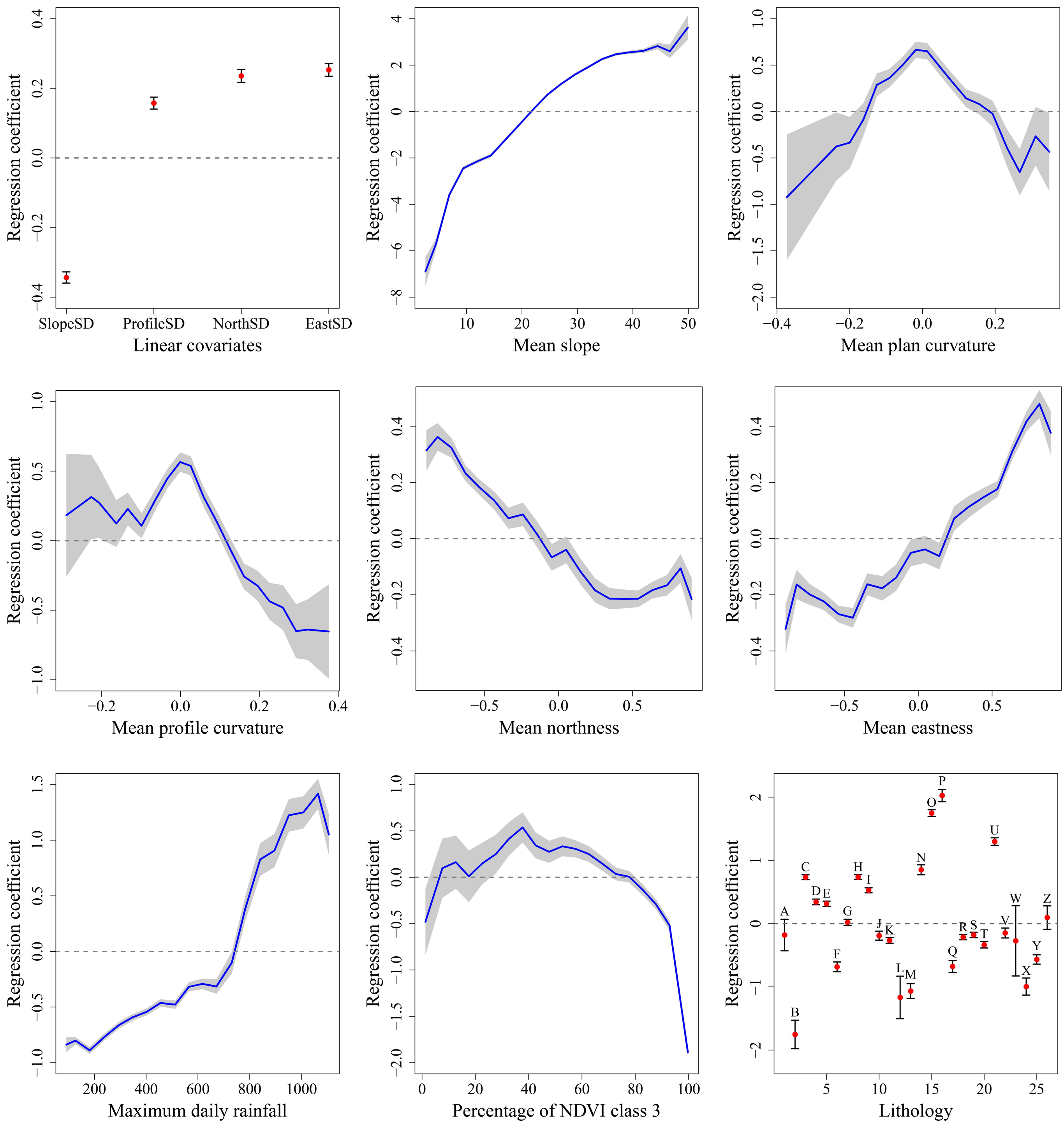


**Fig. 3.** Summary of fixed (linear) and random (nonlinear) effects of all covariates. For

linear effects, the red dots show the posterior mean, and the vertical segments are the 95% credible intervals. For nonlinear effects, the blue curves show the posterior mean, and the shadowed polygons are the 95% credible intervals. For nonlinear effects of lithology, the red dots show the posterior mean, and the vertical segments are the 95% credible intervals.

## 4.3. Space-time predictive performance

As we aim at testing the capacity of our model to predict landslide occurrences in both space and time, the goodness-of-fit presented above does not constitute a suitable metric. For this reason, we implemented a suite of cross-validation (CV) procedures to subset the spatio-temporal domain under study in a number of ways, and each one aimed at providing a slightly different aspect of the prediction capacity of the model we propose. We briefly recall here that a cross-validation routine makes use of a calibration step where we fit the same explanatory model as before, but on a small subset of the spatio-temporal domain under consideration, only to test the classification power on the complementary subset.

We report the results of the five cross-validation schemes detailed in Section 3.5 namely, 10fold-CV, S-CV, T-CV, TF-CV, ST-CV. **Fig. 4** provides an overview of the purely random 10fold-CV, where a mean AUC of 0.845 was estimated, in the same range shown for the goodness-of-fit. Inspection of the boxplot in the right panel indicates that the AUC essentially does not vary as the 10 random subsets are iteratively tested for prediction. We stress here that a purely random 10fold-CV is the most conservative testing method, especially in a large spatio-temporal domain such as ours. In fact, as the samples to be taken out for validation are selected at random, the structure and data arrangement upon which the model is build stays essentially the same, and so does the validation subset. In other words, a purely random 10fold-CV is not suitable to disaggregate the spatial and temporal dependence in the data, which is then reflected in the high performance we retrieved.

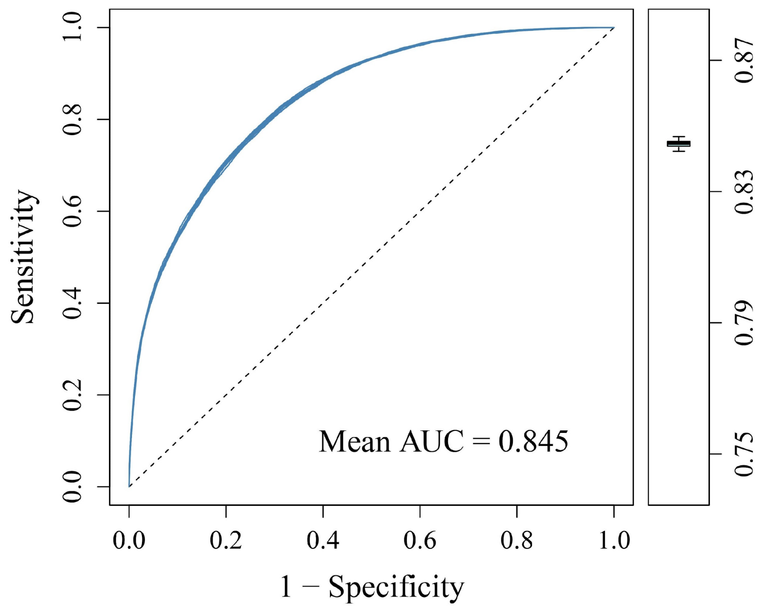


**Fig. 4.** ROC curves obtained via traditional 10-fold CV. The boxplot shows the AUC variation of 10 subsets.

To test the prediction capacity of our models in areas that have never been presented to it, we moved to the S-CV procedure. **Fig. 5** provides an overview, where the model achieved an excellent mean AUC value of 0.803 according to the classification criteria from Hosmer and Lemeshow (2000). However, the model has low AUC values of less than 0.8 in predicting sub-region 1, 3, and 5, whereas it obtains the highest AUC value of 0.873 in predicting sub-region 4. This indicates that the model has low predictive performance in predicting the northeastern Taiwan. Inspection of the boxplots shows the S-CV has a larger AUC fluctuation compared to the 10-fold CV (**Fig. 4**) and the two temporal validation results (**Fig. 5**). This indicates that it is difficult for the model to achieve stable and accurate predictions for all regions. In other words, the geographic variability significantly affects the model predictive performance.

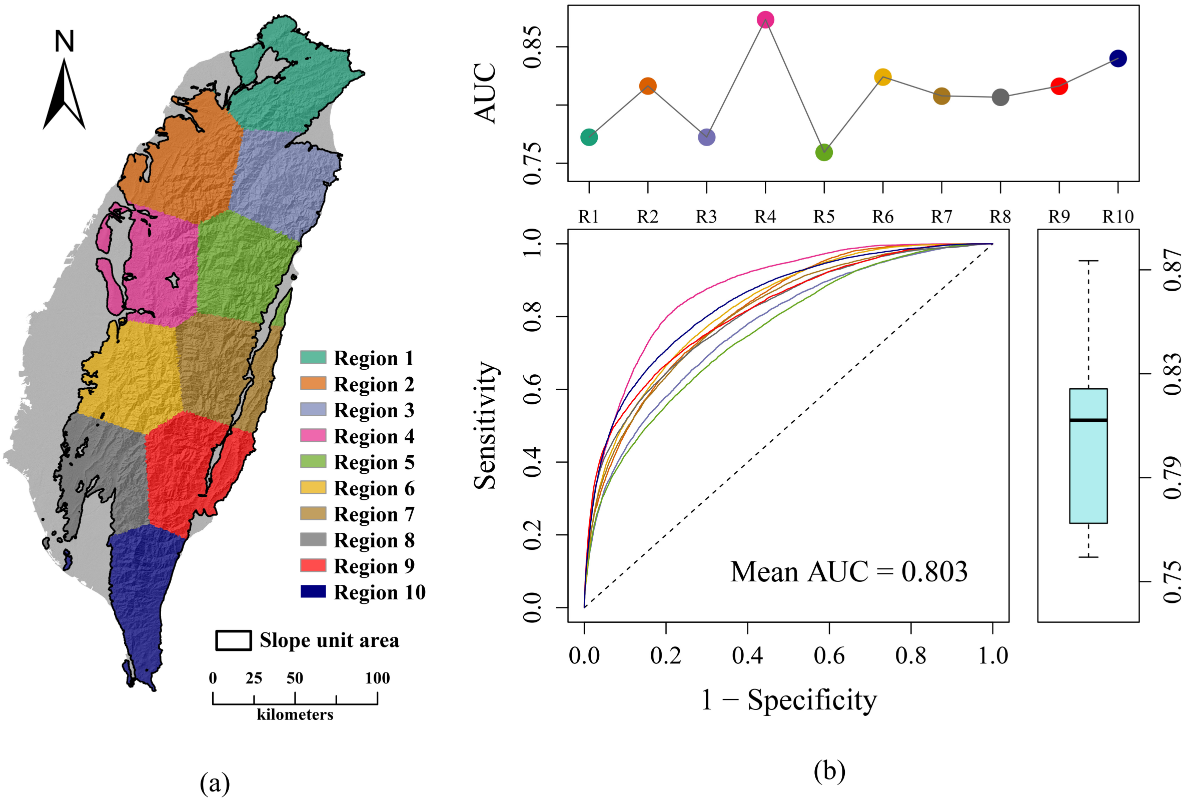


**Fig. 5.** Spatial leave-one-out cross-validation (S-CV) results. (a) 10 spatial sub-regions used for validation and (b) predictive performance assessed using ROC curves. Colored curves and dots denote the performance of different sub-regions. The boxplot summarizes the AUC variation over 10 sub-regions.

The T-CV and TF-CV schemes were used to assess the model predictive performance in the time dimension, and the results are summarized in **Fig. 6**. The models achieve the same mean AUC value of 0.842 by considering the two temporal validation schemes. Both models have the worst predictive performance in predicting data of T5 (2008-2009), and obtain the highest AUC values in T8 (2011-2012). Note that there is no validation result in T1 (2004-2005) for the TF-CV, because this scheme started with T1 and only predicted the next time period. In **Fig. 6** (b), we also presented the AUC values of T-CV as black plots for better comparison. Notably, the T-CV achieves higher AUC values than the model with TF-CV before T9 (2012-2013), and then obtains similar performance after T9. This is because T-CV always considers 13 time periods data for fitting and validates using the left-out one time period, whereas the TF-CV only uses samples of current and past time periods for fitting. Therefore, the number of available fitting samples for TF-CV are much less than that of T-CV in the previous time periods. When the number of fitting samples is large enough (after T9), the performance difference caused by data size is significantly decreased.

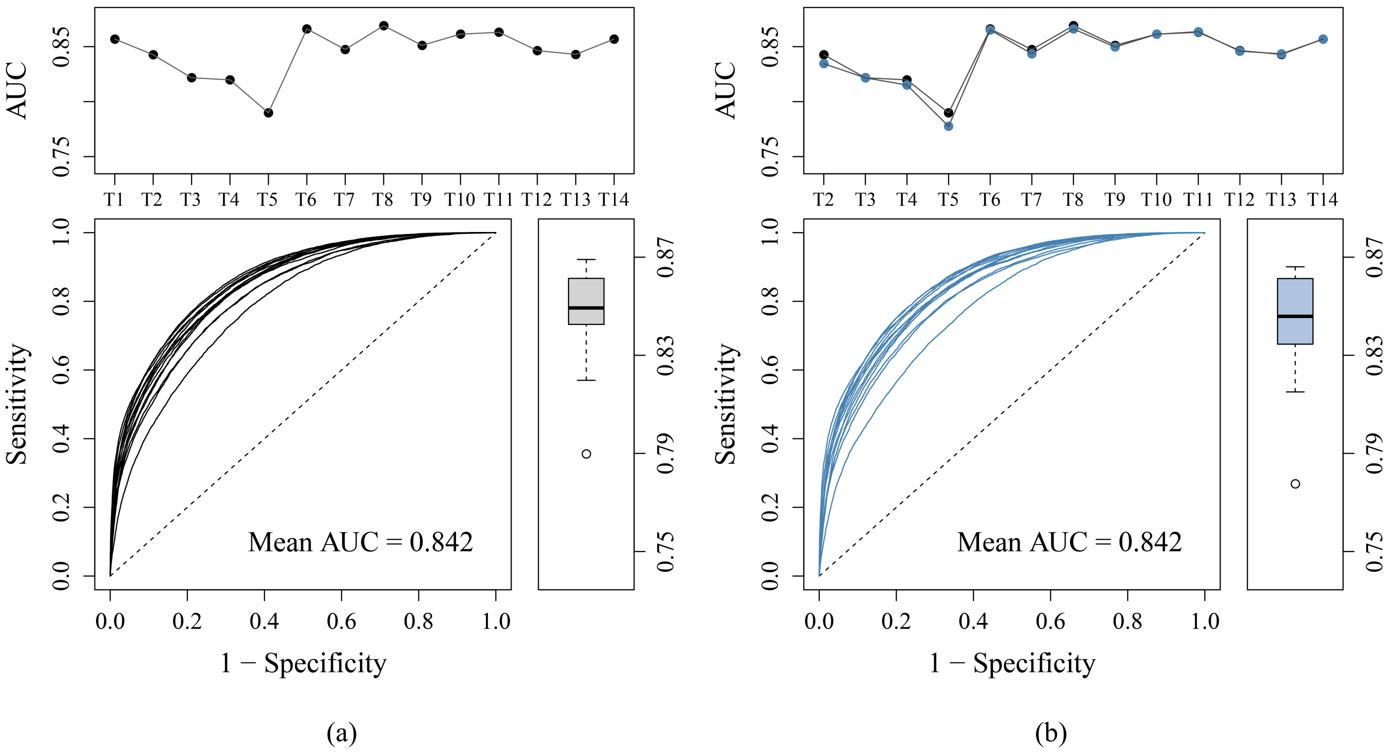


**Fig. 6.** Temporal validation results. (a) Temporal leave-one-out cross-validation (T-CV) and (b) temporal forward validation (TF-CV). Curves and dots denote the performance of different time periods. Boxplots summarize the AUC variation over all time periods. Note that the black dots in panel (b) denote the AUC values of different time periods assessed via T-CV.

In order to assess the model predictive performance in both space and time dimensions, we performed a ST-CV scheme. Specifically, we divided the whole dataset into 140 subsets based on 10 space sub-regions (**Fig. 5** (a)) and 14 time periods. Next, the model is fitted using 139 subsets, and then validated using the left-out subset. This procedure was repeated until all subsets were validated. **Fig. 7** presents the validation results of the ST-CV scheme. The model achieved an excellent mean AUC value of

0.819 by considering 140 ROC curves. Similar to the S-CV validation, the space-time model has low AUC values of less than 0.8 in the northeast of Taiwan (sub-region 1, 3, and 5) (**Fig. 5**), and achieves the highest and most stable results in sub-region 4. Inspection of the boxplots shows that the AUC values of sub-region 1 and 10 has greater fluctuations compared to other sub-regions, indicating a high temporal variability in the two sub-regions. In addition, we can observe that sub-region 2, 4, 6, and 8 shows higher mean AUC values than sub-region 3, 5, 7, and 9, respectively. This means the model achieves better susceptibility prediction results in western part of the study area as compared to the eastern part.

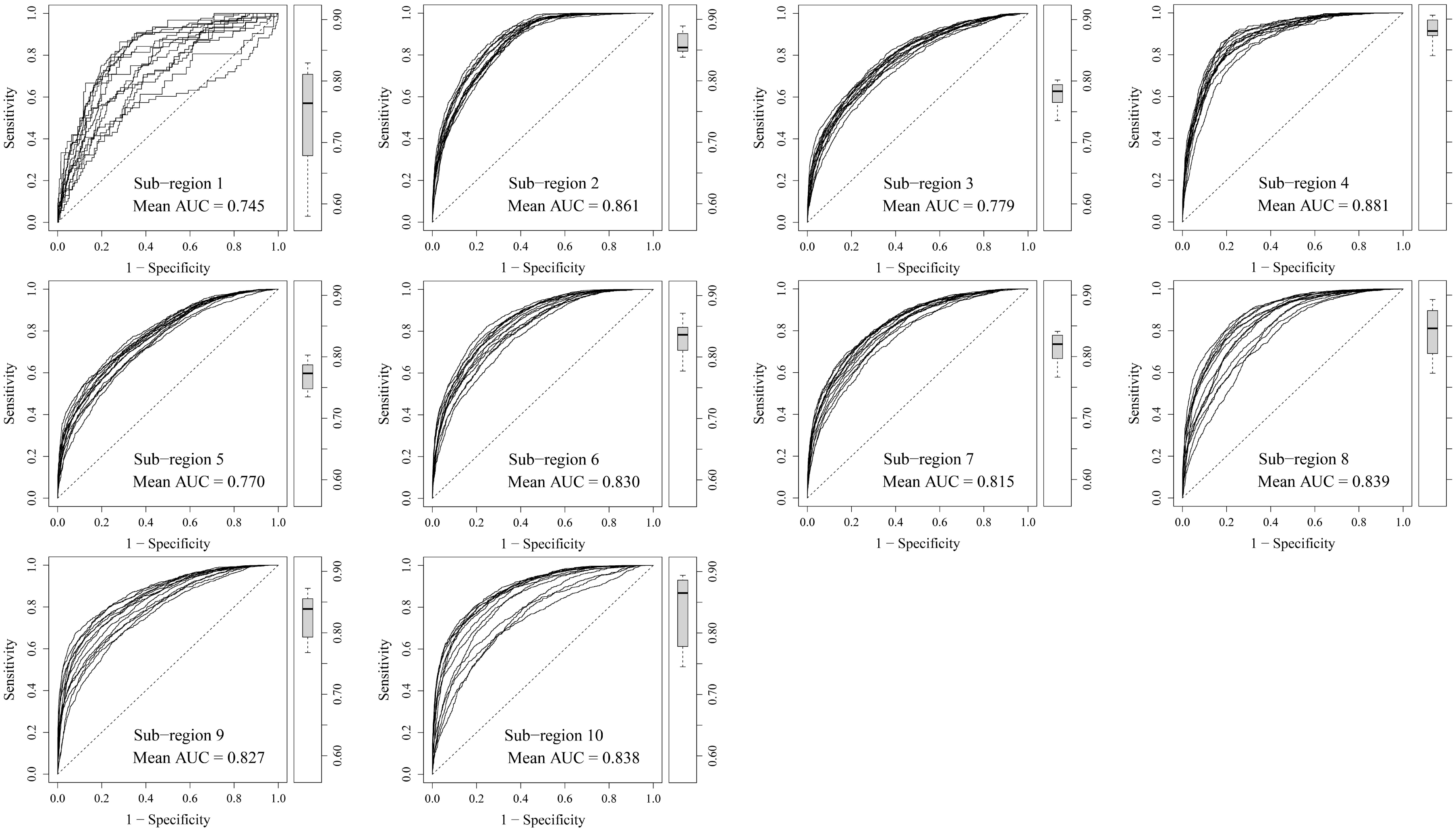


**Fig. 7.** ROC curves obtained via ST-CV. Each panel shows ROC curves for all time periods in the same sub-region. Boxplots summarize the AUC variations for different sub-region over 14 time periods.

## 4.4. Landslide susceptibility maps

The T-CV procedure was used to predict the landslide susceptibility maps of the 14 time periods, as shown in **Fig. 8**. To appropriately illustrate the susceptibility maps, we used the effectiveness ratio to classify continuous values into five meaningful classes (Chung and Fabbri, 2003; Guzzetti et al., 2006). The effectiveness ratio is the ratio of the proportion of landslide areas in each susceptibility category to the proportion of the susceptibility category in the study area. For the whole space-time susceptibility spectrum, we considered an effective class with a ratio at least 4 or less than at least 0.3. For a significantly effective class, the ratio is at least 6 (50% increase) or less than at least 0.15 (50% decrease). Finally, we calculated four cutoff values of 0.193, 0.393, 0.45, and 0.638 to classify the maps into five classes: very low, low, moderate, high, and very high (VL, L, M, H and VH hereafter). Visual inspection of the 14 landslide susceptibility maps shows distinct spatial characteristics and strong spatial variations over time. VH susceptibility areas are mainly distributed in the Central Mountain Range of Taiwan. As for southern part of Taiwan, a peak in VH can be seen appearing in T6 (2009-2010), though it gradually disappeared in the following years. This may be due to the large landslide event caused by Typhoon Morakot in August 2009. **Fig. 9** presents brief statistics of the 14-year landslide susceptibility patterns. The strong difference between maximum and minimum susceptibility estimates implies large variations over time. The mean map smooths these temporal variations, portraying the bulk of the spatial distribution of landslide susceptibility in Taiwan over 14 years.

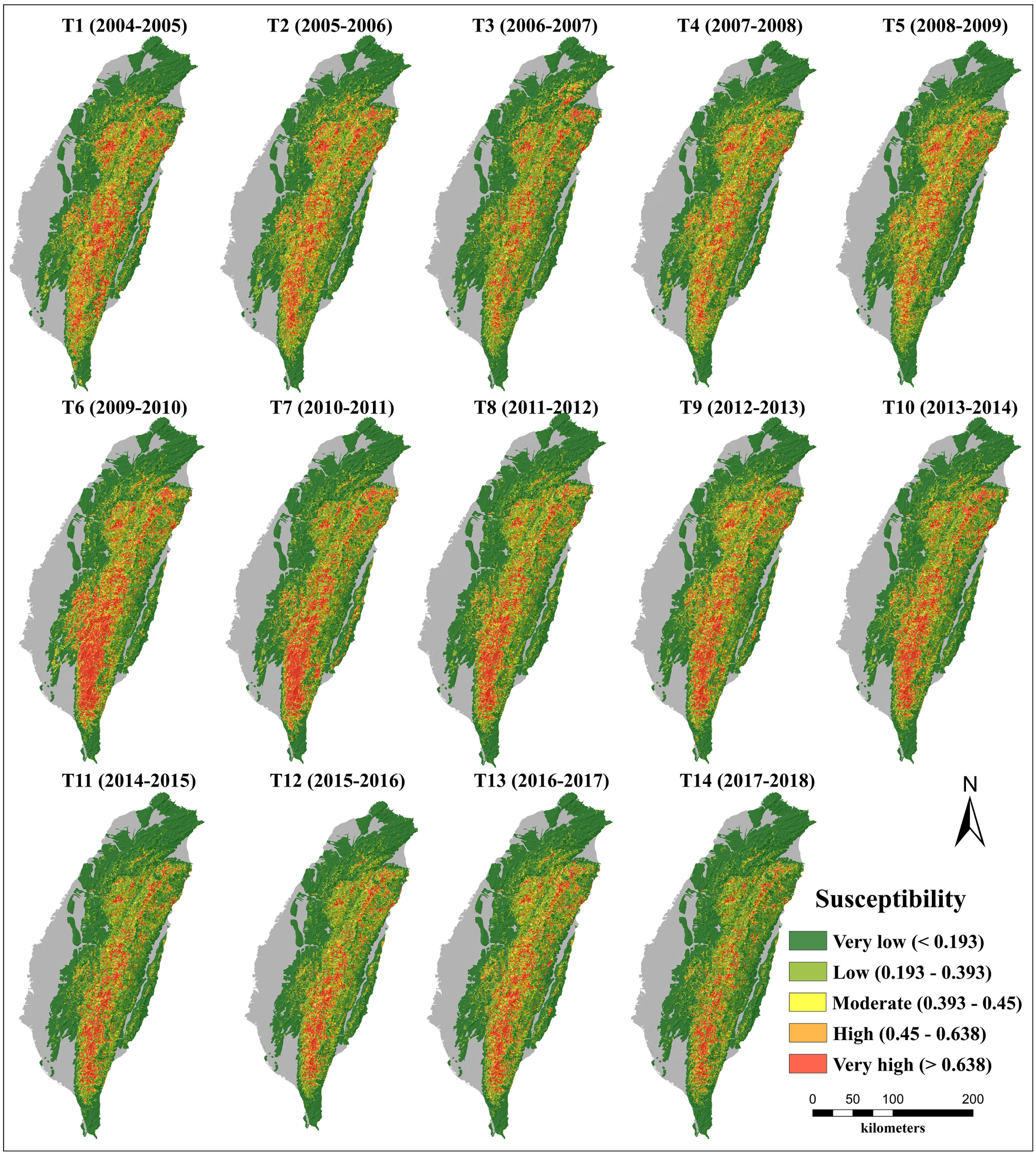


**Fig. 8.** Landslide susceptibility map in Taiwan from 2004 to 2018. The entire time period is divided into 14 shorter time periods, and each is from August 1st of the current year to August 1st of the next year. Continuous susceptibility values are grouped into five classes with equal intervals.

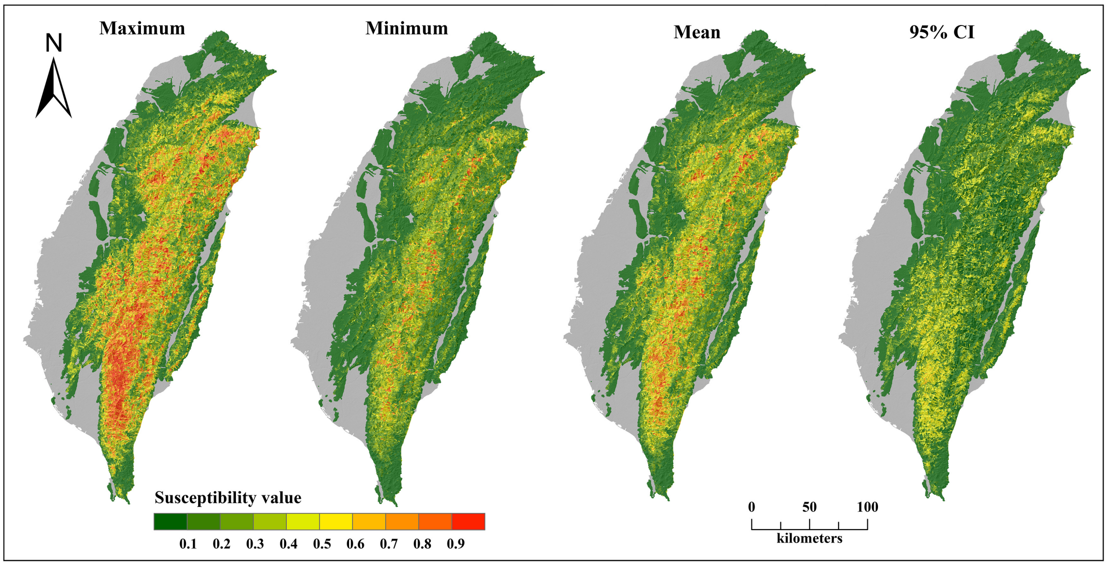


**Fig. 9.** Spatial distribution of the maximum, minimum, mean, and 95% confidence interval (CI) values of landslide susceptibility in Taiwan for the entire period.

**Fig. 10** offers a different perspective, compressing the spatial information into a stacked barplot, where the five classes are shown for their proportional extent with respect to the whole Taiwan. No obvious upward or downward trend among susceptibility levels can be seen, with the exception of T6 (2009-2010). To further investigate the proportions of high and very high susceptibility classes in certain time periods, we also checked typhoon events that have discharged a maximum 24-hour rainfall above 740 mm according to the Typhoon Database of Taiwan. We selected the 740 mm threshold because it represents the transition of the positive regression coefficients in **Fig. 3**. The increase of very high susceptibility area from T3 (2006-2007) to T4 (2007-2008), T4 to T5 (2008-2009), T5 to T6 (2009-2010), and T8 (2011-2012) to T9 (2012-2013) may be associated to the occurrence of new landslides and expansion of old landslides caused by Typhoon Krosa (October 2007), Typhoon Sinlaku (September 2008), Typhoon Morakot (August 2009), and Typhoon Soulik (July 2013), respectively. Moreover, the susceptibility maps for T1 and T7 still contain large unstable (high and very high susceptibility) areas, which may be due to Typhoon

Haitang (July 2005) and Typhoon Megi (September 2009), respectively.

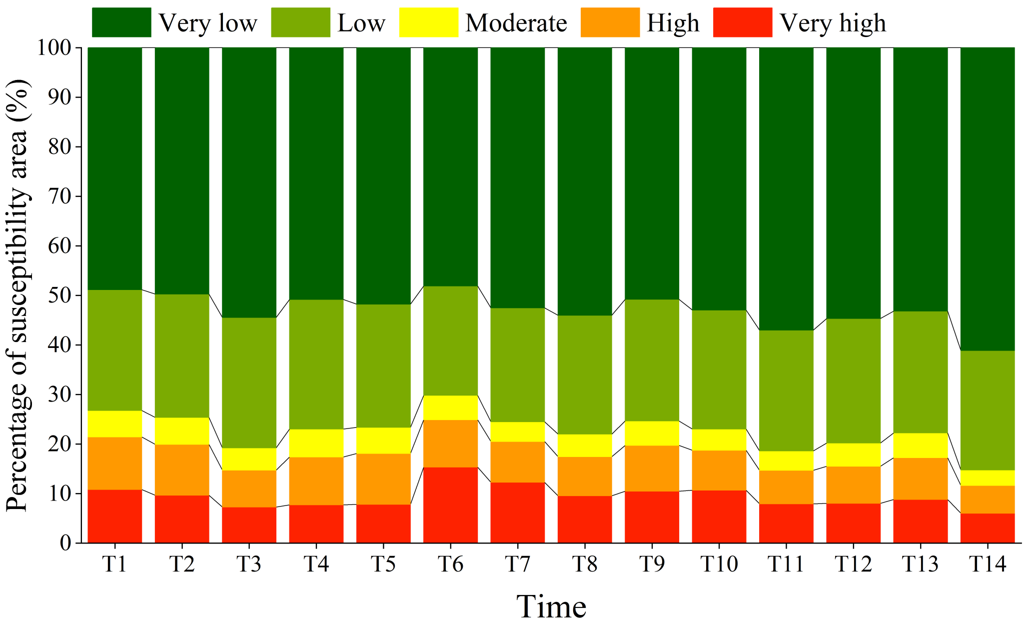


**Fig. 10.** Percentages of different susceptibility areas from T1 to T14.

To inspect the predictive performance of the model from a spatial perspective, we further present the confusion maps in **Fig. 11**. This type of susceptibility summary essentially highlights slope units that have been classified correctly or incorrectly by showing the spatial translation of a confusion matrix (Titti et al., 2022b). This operation returns slopes units falling into four classes: true positive (TP), false negative (FN), false positive (FP), and true negative (TN). The best susceptibility cutoff used to compute the confusion matrix was selected on the basis of the Youden's J statistic (Youden, 1950). Most slope units appear to be correctly predicted as the spatial distribution of TP and TN largely occupied the island, while FN and FP are less represented. An interesting aspect is related to the distribution of FP. These are slope units that the model classified as unstable, although the inventory does not contain landslides at those locations. This information though is not to be considered an error per se, it is actually where the indications of any susceptibility models should be emphasized because even if landslides have not manifested yet, this does not mean that they may not do so in the future.

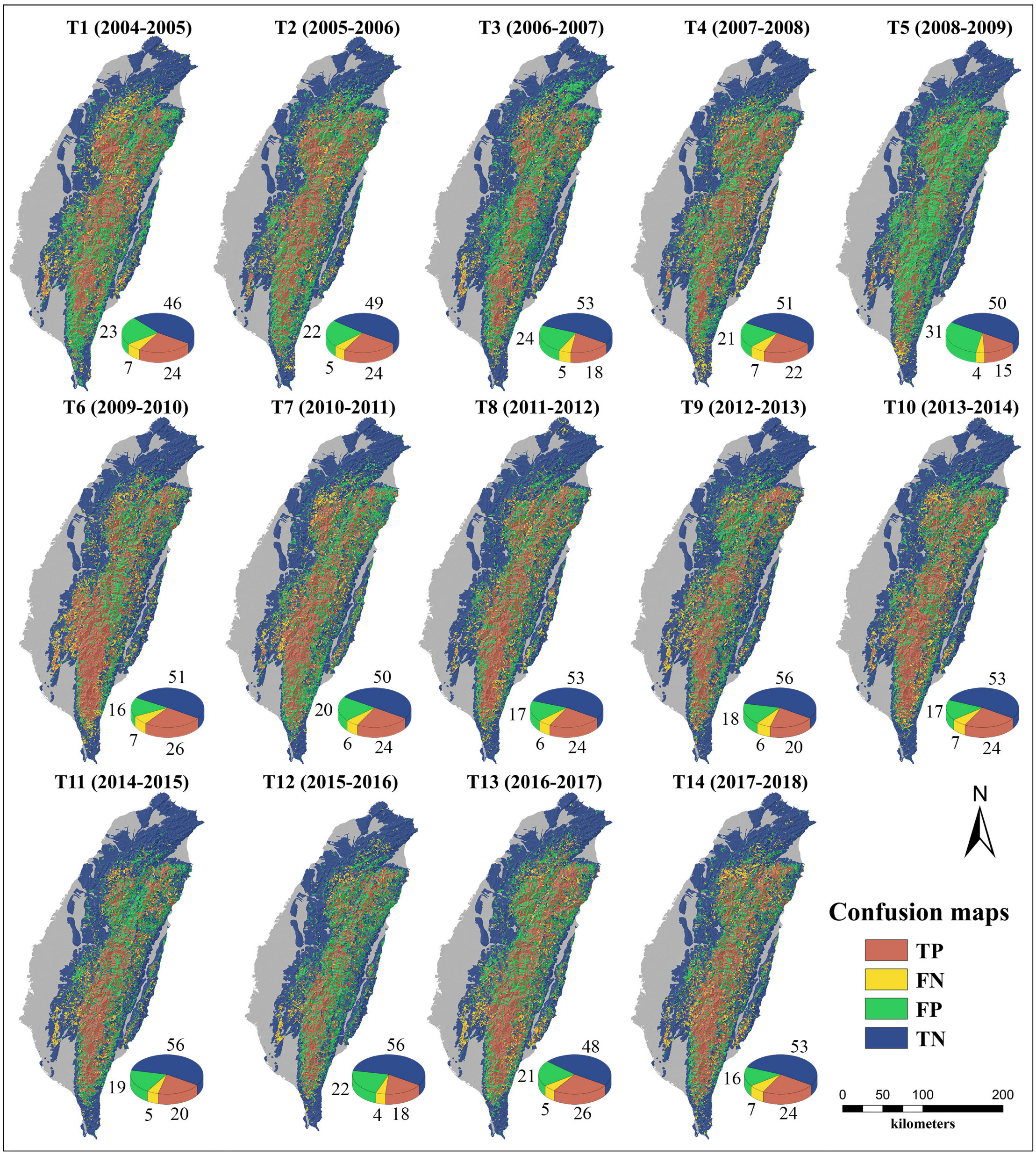


**Fig. 11.** Confusion maps: the pie charts show the percentages of different classes in the maps.

# 5. Discussion

## 5.1. Model performance

In general, landslide susceptibility models should be evaluated both in terms of goodness-of-fit and predictive capacity (Guzzetti et al., 2006; Reichenbach et al., 2018; Lombardo et al., 2020a). The former is meant to assess the ability to explain known landslides and the corresponding model is also used to interpret covariate effects

(Steger et al., 2021a). The latter measures the ability to predict landslides whose information is not part of the fitting procedure. Here, we want to emphasize these two aspects because the concept of prediction in landslide susceptibility studies is often confined to spatial subsets of the same inventory (e.g., Lin et al., 2021). However, being our model contextually build over space and time, we have the chance to explore what "prediction" really meant across the whole spatio-temporal domain. The goodness-of-fit returned a AUC value of 0.845 (**Fig. 2**), an excellent result according to Hosmer and Lemeshow (2000). As for the validation of predictive performance, we presented a full suite of cross-validation routines, some of them returned AUC values not far from the fit, while others indicated significantly lower capacity to

predict landslides under certain conditions. Specifically, we followed and extended the cross-validation routines described in Brenning (2012) in the spatial context and in Wang et al. (2022) for the spatio-temporal one. The 10fold-CV returned performance metrics in line with the goodness-of-fit. Conversely, deviations from the goodness-of-fit become much more evident for the remaining cross-validation. The S-CV returned a mean AUC of 0.805 and a maximum drop in AUC of ~ 0.1, recorded for Region 1, located in the northern island. Both T-CV and TF-CV returned much closer predictive skills to the reference model, with both mean AUC values of 0.842 and a maximum performance drop at T5. As for the ST-CV, among the 140 subsets, Region 1 is associated again with the worst prediction, though the 0.745 mean AUC of the 10 retrieved in this sector still indicates a suitable prediction. This is currently the most complete spatio-temporal prediction overview in the landslide susceptibility literature and it is interesting to note that no matter how we shuffled the dataset, the performance still remained within the excellent prediction class defined by Hosmer and Lemeshow (2000). This has implication beyond the context of landslide susceptibility and even hazard, because if used for risk mitigation purposes, our model would have been able to predict around 80% of the unstable slopes each year. The real issue is that our model is backpropagated to explain something that has already happened in the past and thus still lacks elements of actual prediction. To improve on this aspect, it would be possible to test our model for operational uses, by using it to build scenarios where forecasted or designed rainfall amounts are plugged into the predictive equation we retrieved (Lombardo and Tanyas, 2021). Aside from what can be done and describing more what has already been done in Taiwan, Wu (2015) described the spatial distribution of landslide susceptibility in the Chishan watershed of Taiwan after Typhoon Morakot, and the reported performance reached an AUC of 0.77. Shou and Lin (2016) conducted a landslide susceptibility analysis along a mountain highway in central Taiwan, and the predictive capacity of their model produced ranged from 0.717 to 0.916. Moreover, Lin *et al*. (2017) implemented six different landslide susceptibility models within the Kaoping river basin of Taiwan and their ensemble still led to an AUC of 0.79. Shou and Lin (2020) assessed the landslide susceptibility in the Wu River watershed of Taiwan testing machine learning architectures, resulting in AUC values between 0.754 and 0.8478. This is to say that even compared with traditional static susceptibility model, the increased complexity due to the spatio-temporal nature of our model still produced suitable predictive performance.

## 5.2. Interpretation of covariate effects

In our space-time modelling framework, we performed two preprocessing steps to remove redundant information, select the most informative covariate set and how a variable should enter the modeling routine. The latter consists of a test where we build *n*-single-variable models (*n* is the number of covariates we initially considered), where each covariate was initially introduced to the model as a nonlinear property. If the given variable behaved nonlinearly, then we noted this characteristic for further use. The same was done for covariates that behaved linearly or close to linear. The second preprocessing step was introduced to determine the final covariate combination based on a stepwise-forward selection procedure. The criterion for the selection or rejection of a given covariates was based on the DIC (Spiegelhalter et al., 2002). Specifically, we set a DIC threshold at 100. If the inclusion of a single covariate would not decrease the whole DIC at least by 100, then we considered the covariate non-informative and remove it from the analyses.

The covariate effects we then estimated are presented below in the context of the literature, especially for the already available cases within Taiwan (albeit only within the pure spatial context). Huang *et al*. (2017) analyzed the effects of terrain attributes on landslides from an island-wide perspective in Taiwan, finding that typhoon-induced landslides cluster in areas with terrain slope between 25º and 45º. This result is in agreement with our what we see in **Fig. 3**, where the mean slope presents positive regression coefficients between 22º and 43º.

The profile curvature maintains a negative effect above 0.1, indicating that upwardly concave terrain is less prone to landsliding. This is something that has already been observed in other susceptibility studies (Lombardo et al., 2018), and it is usually interpreted under the assumption that upwardly concave morphologies would experience acceleration in terms of overland flows and thus lead to higher erosion and destabilization capacity (Ohlmacher, 2007). With regards to the slope exposition, we opted for a generally accepted strategy where the terrain aspect is decomposed into northness and eastness (Cama et al., 2017; Lombardo et al., 2020a; Samia et al., 2020; Bryce et al., 2022). Among the available contributions in Tawain, Lee (2013) indicated that slopes facing south and southeast hosted more frequently landslides than others during the Chi-Chi earthquake. However, such observation may be due to ground motion directivity effects. Nevertheless, Chen *et al*. (2019a) also noted that landslide prone slopes faced east, southeast, and south directions. These results well agree with our own, for we estimated south- and east- facing slopes to be more susceptible.

Leaving behind static or time-invariant covariates, below we will comment on the dynamic variables we integrated in our dynamic susceptibility model. Chen *et al*. (2013) investigated the relationship between landslide erosions and nine rainfall variables based on 24 rainfall events in three mountainous watersheds in Taiwan. They found that the maximum 24-hour rainfall was more correlated with landslides that any other rainfall expression in time. Wei et al. (2018) analyzed 941 landslides cases and investigated their relationships with rainfall indices, concluding that 24-hour rainfall was also the most dominant long-term variable for rainfall-induced landslides in Taiwan. In our case though, as our model spans until 2004, obtaining hourly rainfall data for the entirety of Taiwan and for the whole time domain was not possible. We therefore used the maximum daily rainfall to express the climatic control on landslide susceptibility. Chen et al. (2015) found that a 24-hour rainfall exceeding 710 mm could induce high landslide erosion rates in Kaoping catchment of Taiwan. Lee et al. (2016) set the 24-hour rainfall and 3-hour rainfall intensity as 500 mm and 50mm/h as their suitable thresholds to determine high alert level based on 941 shallow landslides in Taiwan. Huang et al. (2017) indicated that landslides triggered by Typhoon Morakot are more likely to occur when the rainfall exceeds 600 mm per day. In our study, we found that the regression coefficient increases with the increase of the maximum daily rainfall. Moreover, the maximum daily rainfall shows a positive contribution to the model for rainfall values greater than 740 mm per day. Differences with respect to the literature mentioned above should be place into context, as all these studies focused on single or few catchments at best, whereas our work covers the whole island.

NDVI is another dynamic covariate used in our study, which can reflect surface conditions from bare lands to highly vegetated slopes. We modelled the effect of NDVI with three discrete classes instead of continuous values because our target variable is landslide expansion areas in each time period. This process can partially eliminate the undesired effect of pre-existed landslide scars. The third NDVI class shows a significant and negative effect on the susceptibility for SUs covered by vegetation for more than 70% of their extent. This is geomorphologically reasonable because high vegetation cover could reduce soil erosion and thus limit runoff-induced failures (Fan et al., 2021). As for the lithology, class B (Pleistocene andesite) was estimated with the highest negative effect on landslide occurrences whereas the classes P, O, and U (respectively representing mudstone, shale, and sandstone) were associated with positive regression coefficients, well above to 1. This is in agreement with the study by Wu and Chen (2009) where the authors highlighted that igneous rocks are associated with a low landslide frequency, whereas sandstone, shale, and mudstone are attributed the highest landslide rates in central Taiwan.

Notably, no earthquake-related covariates passed the initial variable selection routine and this came as a surprise. We collated 56 PGA maps from the USGS ShakeMap system (Worden and Wald, 2016), all corresponding to earthquakes with magnitude above 5.0, occurred within the spatio-temporal domain examined in this work. Thus, our initial assumption was that the effect of ground motion, be it direct or preparatory via legacy processes (Tanyaş et al., 2021). However, it appeared that the ground motion signal did not provide any explanatory information which in turn may imply that the primary landslide trigger for the period we examined uniquely consist of heavy and/or persistent rainfall.

## 5.3. Generation of susceptibility maps

In landslide susceptibility studies, it is common to group the continuous susceptibility values into several meaningful classes. However, there is no consensus on which scheme to use for reclassification (Reichenbach et al., 2018). In this study, we concatenated all the space-time susceptibility values into a single vector and determined corresponding cut-off values based on the effectiveness ratio. Chung and Fabbri (2003) considered a significant prediction class should retain a ratio of effectiveness at least larger than 3 or less than 0.2, and a significantly effective class should keep the ratio larger than 6 or less than 0.1. Guzzetti et al. (2006) indicated that the above criteria are difficult to match, and regarded four effectiveness ratio values of 3, 1.5, 0.5, and 0.25 in the Collazzone area, central Italy. Considering the space and time ranges of our study, we considered the ratio of an effective prediction class to be at least larger than 4 or less than 0.3, and a corresponding 50% increase or 50% decrease for a significantly effective class. Having opted for this classification criterion, we ultimately applied it on the landslide susceptibility maps produced via the T-CV procedure, on a yearly basis (**Fig. 8**). We stress that the generation of a slope unit partition excluded flat and near-flat areas. There are shown in grey and we can see as trivial areas where landslide cannot manifest due to unsuitable terrain characteristics. As for the other landslide susceptibility classes, we noticed that the very low one essentially occupied the same regions across different time periods. As for the other extreme represented by very high susceptibility areas, these mostly exhibited spatiotemporal variations in southern Taiwan, mostly due to the influence of Typhoon Morakot. This was the most severe typhoon in the past five decades in Taiwan (Huang et al., 2017), thus its passage across the south explains the rapid increase in landslide occurrences in T6 as well as the resulting susceptibility decay in the following years.

An interesting perspective we provided is brought by the confusion maps shown in **Fig. 11**. These maps present not only the distributions of correctly predicted slope units, but also the spatiotemporal locations of FP and FN. Note that these two types of errors convey different indications for practical purposes (Carrara et al., 1991; Reichenbach et al., 2018). FP indicates slope units unaffected by landslides that have been classified as unstable. As for FN they represent slope units affected by landslides but predicted to be stable. With regards to FP, Carrara et al. (1991) argued that this error may occur because landslides may be covered by erosion or farming activities, in turn implying that a misclassification could be justified because of errors in the initial mapping procedure. In our study, the time interval is just one year. Therefore, landslides must still be visible for the automatic landslide mapping routine and the later verification carried out by Lin et al. (2013). As a result, and as mentioned in Section 4.4, we rather interpret the relatively high number of FP produced by our model as locations that have not yet exhibited slope instability but may potentially do so in the future. In this sense, one may argue that being the nature of our model spatio-temporal, these FP could still be considered an indication of a classification error. However, a slope failure is a rare event in a given landscape and a FP should still be considered an important indication rather than an error per se, as they may still provide insightful information on which slope units may require stabilization or at least should not be assigned as urban development areas in local master plans. In other words, looking at **Fig. 11** the average percentage of FP across maps is 21% of the Taiwanese island. This means that those 21% of SUs are the ones requiring further attention.

As for the FN, these are real errors, as they represent misclassified slope units that were actually hosting one or more landslides in time. However, the numbers are always confined below 8%, which in turn stresses once more the prediction ability of our space-time classifier.

# 6. Conclusions

We implemented a space-time version of a susceptibility model in the main island of Taiwan from 2004 to 2018. The spatial partition relied on a slope unit delineation whereas the temporal partition relied on a yearly time step. This implies that we generated a dynamic susceptibility pattern varying over Taiwan on a yearly basis. The model was tested both in its explanatory and predictive capacities. The latter actually corresponds to the most complete suite of cross-validation routines currently available within the landslide susceptibility literature. The results indicate that knowing both the time-invariant information of the terrain characteristics as well as the time-variant information of vegetation density and rainfall is enough to suitably classify the mapping units prone to slope failure in Taiwan. This is a promising step towards an operational use of this dynamic susceptibility estimates. However, to convert this model into an operational one, the temporal units needs to be significantly shortened, from the yearly unit in this work to ideally a landslide event-based characteristic. To do so, also event-based inventories are required, which is something that has not yet been achieved in Taiwan, at least for the whole extent of the island and for a relevant time series. In the future, we expect this step to be possible, especially thanks to the increased frequency in orbital acquisition of satellite images as well as the consolidation of automatic mapping routine within the geoscientific community. Another potential improvement to be explored corresponds to modeling a different landslide characteristic. Recent contributions have shown that aside from the traditional susceptibility context, the extent of landslides within a given mapping unit can also be suitably predicted. This information can complement the dynamic susceptibility presented in this study. When the multi-temporal landslides are mapped as polygons, it will be possible to create the first space-time predictive model of landslide sizes, which is also something we have already started to explore. Overall, we believe that probabilistic space-time landslide prediction models will be the next generation of data-driven architectures to be pursued by the landslide community and we consider this work a forerunner among the scientific contribution in this topic.

# Acknowledgement

This work was supported by the Joint Funds of the National Natural Science Foundation of China (U21A2013), the State Key Laboratory of Biogeology and Environmental Geology, China University of Geosciences (GBL12107), the National Natural Science Foundation of China (61271408), the China Scholarship Council (No. 202106410043), and the Fundamental Research Funds for National Universities, China University of Geosciences (Wuhan). This article was also partially supported by King Abdullah University of Science and Technology (KAUST) in Thuwal, Saudi Arabia, Grant URF/1/4338-01-01. We also thank the Taiwanese scientists that made the input data freely available.

# Data and codes availability statement

The data and codes that support the findings of this study can be accessed at: https://doi.org/10.6084/m9.figshare.20237718.

# Appendix A. Description of different time periods

| Time period | Description |
| --- | --- |
| T1 | Landslides from 1st August 2004 to 31st July 2005 |
| T2 | Landslides from 1st August 2005 to 31st July 2006 |
| T3 | Landslides from 1st August 2006 to 31st July 2007 |
| T4 | Landslides from 1st August 2007 to 31st July 2008 |
| T5 | Landslides from 1st August 2008 to 31st July 2009 |
| T6 | Landslides from 1st August 2009 to 31st July 2010 |
| T7 | Landslides from 1st August 2010 to 31st July 2011 |
| T8 | Landslides from 1st August 2011 to 31st July 2012 |
| T9 | Landslides from 1st August 2012 to 31st July 2013 |
| T10 | Landslides from 1st August 2013 to 31st July 2014 |
| T11 | Landslides from 1st August 2014 to 31st July 2015 |
| T12 | Landslides from 1st August 2015 to 31st July 2016 |
| T13 | Landslides from 1st August 2016 to 31st July 2017 |
| T14 | Landslides from 1st August 2017 to 31st July 2018 |

# Appendix B. Summary of lithology class

| Class | Description |
| --- | --- |
| A | Miocene andesite |
| B | Pleistocene andesite |
| C | Eocene phyllite, slate, and sandstone |
| D | Eocene to Oligocene quartzite, slate and phyllite |
| E | Oligocene to Miocene hard shale, slate, and phyllite |
| F | Early Miocene agglomerate and tuffaceous sandstone |
| G | Middle Miocene sandstone and shale |
| H | Miocene hard shale, slate, and sandstone |
| I | Late Miocene sandstone and shale |
| J | Early Miocene sandstone and shale |
| K | Oligocene to Miocene hard shale, sandy shale, and sandstone |
| L | Oligocene to Miocene sandstone, shale, and coaly shale |
| M | Oligocene to Miocene hard shale, slate, phyllite, sandy shale, and sandstone |
| N | Pliocene shale, sandy shale, and mudstone |
| O | Pliocene sandstone, mudstone, and shale |
| P | Pliocene to Pleistocene mudstone and allochthon |
| Q | Late Paleozoic to Mesozoic gneiss |
| R | Late Paleozoic to Mesozoic marble |
| S | Late Paleozoic to Mesozoic black schist, green schist, and metachert |
| T | Late Paleozoic to Mesozoic black schist |
| U | Late Miocene to Pliocene shale, siltstone, sandstone |
| V | Pliocene to Pleistocene sandstone, mudstone, and shale |
| W | Pleistocene limestone |
| X | Pleistocene lateritic terrace deposits |
| Y | Recent alluvium |
| Z | Tertiary mafic igneous rock |

# References


Aguilera, Q., Lombardo, L., Tanyas, H., Lipani, A., 2022. On the prediction of landslide occurrences and sizes via Hierarchical Neural Networks. Stoch. Env. Res. Risk. A.

Alvioli, M., Guzzetti, F., Marchesini, I., 2020. Parameter-free delineation of slope units and terrain subdivision of Italy. Geomorphology, 107124.

Alvioli, M. et al., 2016. Automatic delineation of geomorphological slope units with r. slopeunits v1. 0 and their optimization for landslide susceptibility modeling. Geoscientific Model Development, 9, 3975.

Atkinson, P.M., Massari, R., 1998. Generalised linear modelling of susceptibility to landsliding in the central Apennines, Italy. Comput. Geosci., 24, 373-385.

Bakka, H., Vanhatalo, J., Illian, J.B., Simpson, D., Rue, H., 2019. Non-stationary Gaussian models with physical barriers. Spatial statistics, 29, 268-288.

Bradley, A.P., 1997. The use of the area under the ROC curve in the evaluation of machine learning algorithms. Pattern. Recogn., 30, 1145-1159.

Brenning, A., 2012. Spatial cross-validation and bootstrap for the assessment of prediction rules in remote sensing: The R package sperrorest, 2012 IEEE international geoscience and remote sensing symposium. IEEE, pp. 5372-5375.

Broeckx, J. et al., 2020. Landslide mobilization rates: A global analysis and model. Earth-sci. Rev., 201, 102972.

Bryce, E., Lombardo, L., van Westen, C., Tanyas, H., Castro-Camilo, D., 2022. Unified landslide hazard assessment using hurdle models: a case study in the Island of Dominica. Stoch. Env. Res. Risk. A., 1-14.

Calcaterra, D., Di Martire, D., Palma, B., Parise, M., 2010. Assessing landslide risk through unique condition units. Williams AL, Pinches GM & Chin CY, Geologically Active: Proceedings of the ….

Cama, M., Lombardo, L., Conoscenti, C., Rotigliano, E., 2017. Improving transferability strategies for debris flow susceptibility assessment: Application to the Saponara and Itala catchments (Messina, Italy). Geomorphology, 288, 52-65.

Carrara, A., 1983. Multivariate models for landslide hazard evaluation. Journal of the International Association for Mathematical Geology, 15, 403-426.

Carrara, A. et al., 1991. GIS techniques and statistical models in evaluating landslide hazard. Earth. Surf. Proc. Land, 16, 427-445.

Chang, C.-T., Wang, H.-C., Huang, C.-y., 2018. Assessment of MODIS-derived indices (2001–2013) to drought across Taiwan's forests. Int. J. Biometeorol., 62, 809-822.

Chen, C.-W. et al., 2019a. Assessing landslide characteristics in a changing climate in northern Taiwan. Catena, 175, 263-277.

Chen, L., Guo, Z., Yin, K., Shrestha, D.P., Jin, S., 2019b. The influence of land use and land cover change on landslide susceptibility: a case study in Zhushan Town, Xuan'en County (Hubei, China). Nat. Hazards Earth Syst. Sci., 19, 2207-2228.

Chen, T.-H.K., Prishchepov, A.V., Fensholt, R., Sabel, C.E., 2019c. Detecting and monitoring long-term landslides in urbanized areas with nighttime light data and multi-seasonal Landsat imagery across Taiwan from 1998 to 2017. Remote Sens. Environ., 225, 317-327.

Chen, Y.-c., Chang, K.-t., Lee, H.-y., Chiang, S.-h., 2015. Average landslide erosion rate at the watershed scale in southern Taiwan estimated from magnitude and frequency of rainfall. Geomorphology, 228, 756-764.

Chen, Y.C., Chang, K.t., Chiu, Y.J., Lau, S.M., Lee, H.Y., 2013. Quantifying rainfall controls on catchment-scale landslide erosion in Taiwan. Earth. Surf. Proc. Land, 38, 372-382.

Chiang, S.-H., Chang, K.-T., 2009. Application of radar data to modeling rainfall-induced landslides. Geomorphology, 103, 299-309.

Chung, C.-J.F., Fabbri, A.G., 2003. Validation of spatial prediction models for landslide hazard mapping. Nat. Hazards, 30, 451-472.

Corominas, J. et al., 2014. Recommendations for the quantitative analysis of landslide risk. Bull. Eng. Geol. Environ., 73, 209-263.

Diodato, N., 2005. The influence of topographic co-variables on the spatial variability of precipitation over small regions of complex terrain. Int. J. Climatol., 25, 351-363.

Fan, X. et al., 2021. Rapidly evolving controls of landslides after a strong earthquake and implications for hazard assessments. Geophys. Res. Lett., 48, e2020GL090509.

Fang, Z., Wang, Y., Peng, L., Hong, H., 2020. Integration of convolutional neural network and

conventional machine learning classifiers for landslide susceptibility mapping. Comput. Geosci., 139, 104470.
Fang, Z., Wang, Y., Peng, L., Hong, H., 2021. A comparative study of heterogeneous ensemble-learning techniques for landslide susceptibility mapping. Int. J. Geogr. Inf. Sci., 35, 321-347.
Fell, R. et al., 2008. Guidelines for landslide susceptibility, hazard and risk zoning for land-use planning. Eng. Geol., 102, 99-111.
Goetz, J.N., Guthrie, R.H., Brenning, A., 2011. Integrating physical and empirical landslide susceptibility models using generalized additive models. Geomorphology, 129, 376-386.
Goovaerts, P., 2000. Geostatistical approaches for incorporating elevation into the spatial interpolation of rainfall. J. Hydrol., 228, 113-129.
Gorsevski, P.V., Gessler, P.E., Boll, J., Elliot, W.J., Foltz, R.B., 2006. Spatially and temporally distributed modeling of landslide susceptibility. Geomorphology, 80, 178-198.
Guzzetti, F., Carrara, A., Cardinali, M., Reichenbach, P., 1999. Landslide hazard evaluation: a review of current techniques and their application in a multi-scale study, Central Italy. Geomorphology, 31, 181-216.
Guzzetti, F., Reichenbach, P., Ardizzone, F., Cardinali, M., Galli, M., 2006. Estimating the quality of landslide susceptibility models. Geomorphology, 81, 166-184.
Hao, L. et al., 2020. Constructing a complete landslide inventory dataset for the 2018 monsoon disaster in Kerala, India, for land use change analysis. Earth system science data, 12, 2899-2918.
Heerdegen, R.G., Beran, M.A., 1982. Quantifying source areas through land surface curvature and shape. J. Hydrol., 57, 359-373.
Hosmer, D., Lemeshow, S., 2000. Applied logistic regression, Second edition. Wiley, New York.
Hua, Y., Wang, X., Li, Y., Xu, P., Xia, W., 2020. Dynamic development of landslide susceptibility based on slope unit and deep neural networks. Landslides.
Huang, J.C. et al., 2017. Terrain attributes of earthquake-and rainstorm-induced landslides in orogenic mountain Belt, Taiwan. Earth. Surf. Proc. Land, 42, 1549-1559.
Hung, J.-J., 2000. Chi-Chi earthquake induced landslides in Taiwan. Earthquake Engineering and Engineering Seismology, 2, 25-33.
Jasiewicz, J., Stepinski, T.F., 2013. Geomorphons—a pattern recognition approach to classification and mapping of landforms. Geomorphology, 182, 147-156.
Khazai, B., Sitar, N., 2004. Evaluation of factors controlling earthquake-induced landslides caused by Chi-Chi earthquake and comparison with the Northridge and Loma Prieta events. Eng. Geol., 71, 79-95.
Krainski, E. et al., 2018. Advanced spatial modeling with stochastic partial differential equations using R and INLA. Chapman and Hall/CRC.
Lee, C.-T., 2013. Re-evaluation of factors controlling landslides triggered by the 1999 Chi–Chi earthquake, Earthquake-induced landslides. Springer, pp. 213-224.
Lee, C. et al., 2016. Combining rainfall parameter and landslide susceptibility to forecast shallow landslide in Taiwan. Geotechnical Engineering Journal of the SEAGS & AGSSEA, 47, 72-82.
Lima, P., Steger, S., Glade, T., 2021. Counteracting flawed landslide data in statistically based landslide susceptibility modelling for very large areas: a national-scale assessment for Austria. Landslides, 18, 3531-3546.
Lin, C.-W. et al., 2011. Landslides triggered by the 7 August 2009 Typhoon Morakot in southern Taiwan. Eng. Geol., 123, 3-12.
Lin, E., Liu, C., Chang, C., Cheng, I., Ko, M., 2013. Using the formosat-2 high spatial and temporal resolution multispectral image for analysis and interpretation landslide disasters in taiwan. J. Photogramm. Remote Sens, 17, 31-51.
Lin, G.-F., Chang, M.-J., Huang, Y.-C., Ho, J.-Y., 2017. Assessment of susceptibility to rainfall-induced landslides using improved self-organizing linear output map, support vector machine, and logistic regression. Eng. Geol., 224, 62-74.
Lin, Q. et al., 2021. National-scale data-driven rainfall induced landslide susceptibility mapping for China by accounting for incomplete landslide data. Geosci. Front., 12, 101248.
Loche, M. et al., 2022. Surface temperature controls the pattern of post-earthquake landslide activity. Scientific Reports, 12, 988.
Lombardo, L., Mai, P.M., 2018. Presenting logistic regression-based landslide susceptibility results. Eng. Geol., 244, 14-24.
Lombardo, L., Opitz, T., Ardizzone, F., Guzzetti, F., Huser, R., 2020a. Space-time landslide predictive modelling. Earth-sci. Rev., 103318.
Lombardo, L., Opitz, T., Huser, R., 2018. Point process-based modeling of multiple debris flow landslides using INLA: an application to the 2009 Messina disaster. Stoch. Env. Res. Risk. A.,

32, 2179-2198.
Lombardo, L., Tanyas, H., 2020. Chrono-validation of near-real-time landslide susceptibility models via plug-in statistical simulations. Eng. Geol., 278, 105818.
Lombardo, L., Tanyas, H., 2021. From scenario-based seismic hazard to scenario-based landslide hazard: fast-forwarding to the future via statistical simulations. Stoch. Env. Res. Risk. A., 1-14.
Lombardo, L., Tanyas, H., Huser, R., Guzzetti, F., Castro-Camilo, D., 2021. Landslide size matters: A new data-driven, spatial prototype. Eng. Geol., 106288.
Lombardo, L., Tanyas, H., Nicu, I.C., 2020b. Spatial modeling of multi-hazard threat to cultural heritage sites. Eng. Geol., 277, 105776.
Manconi, A., Giordan, D., 2016. Landslide failure forecast in near-real-time. Geomatics, Natural Hazards and Risk, 7, 639-648.
Marjanović, M., Kovačević, M., Bajat, B., Voženílek, V., 2011. Landslide susceptibility assessment using SVM machine learning algorithm. Eng. Geol., 123, 225-234.
Meijerink, A., 1988. Data acquisition and data capture through terrain mapping units. ITC journal, 23-44.
Meusburger, K., Alewell, C., 2009. On the influence of temporal change on the validity of landslide susceptibility maps. Nat. Hazards Earth Syst. Sci., 9, 1495-1507.
Monsieurs, E., Dewitte, O., Demoulin, A., 2019. A susceptibility-based rainfall threshold approach for landslide occurrence. Nat. Hazards Earth Syst. Sci., 19, 775-789.
Montgomery, D.R., Dietrich, W.E., 1994. A physically based model for the topographic control on shallow landsliding. Water Resour. Res., 30, 1153-1171.
Ohlmacher, G.C., 2007. Plan curvature and landslide probability in regions dominated by earth flows and earth slides. Eng. Geol., 91, 117-134.
Petschko, H., Brenning, A., Bell, R., Goetz, J., Glade, T., 2014. Assessing the quality of landslide susceptibility maps--case study Lower Austria. Nat. Hazards Earth Syst. Sci., 14.
Reichenbach, P., Mondini, A., Rossi, M., 2014. The influence of land use change on landslide susceptibility zonation: the Briga catchment test site (Messina, Italy). Environ. Manage., 54, 1372-1384.
Reichenbach, P., Rossi, M., Malamud, B., Mihir, M., Guzzetti, F., 2018. A review of statistically-based landslide susceptibility models. Earth-sci. Rev., 180, 60-91.
Rossi, M. et al., 2019. A predictive model of societal landslide risk in Italy. Earth-sci. Rev., 196, 102849.
Rue, H., Martino, S., Chopin, N., 2009. Approximate Bayesian inference for latent Gaussian models by using integrated nested Laplace approximations. Journal of the royal statistical society: Series b (statistical methodology), 71, 319-392.
Saito, H., Uchiyama, S., Teshirogi, K., 2022. Rapid vegetation recovery at landslide scars detected by multitemporal high-resolution satellite imagery at Aso volcano, Japan. Geomorphology, 398, 107989.
Samia, J. et al., 2020. Dynamic path-dependent landslide susceptibility modelling. Nat. Hazards Earth Syst. Sci., 20, 271-285.
Samia, J. et al., 2017. Characterization and quantification of path dependency in landslide susceptibility. Geomorphology, 292, 16-24.
Scheidl, C. et al., 2020. The influence of climate change and canopy disturbances on landslide susceptibility in headwater catchments. Sci. Total. Environ., 742, 140588.
Seijmonsbergen, A.C., 2013. 14.4 The Modern Geomorphological Map. in: Shroder, J.F. (Ed.), Treatise on Geomorphology. Academic Press, San Diego, pp. 35-52.
Shou, K.-J., Lin, J.-F., 2016. Multi-scale landslide susceptibility analysis along a mountain highway in Central Taiwan. Eng. Geol., 212, 120-135.
Shou, K.-J., Lin, J.-F., 2020. Evaluation of the extreme rainfall predictions and their impact on landslide susceptibility in a sub-catchment scale. Eng. Geol., 265, 105434.
Shu, H. et al., 2019. Relation between land cover and landslide susceptibility in Val d'Aran, Pyrenees (Spain): historical aspects, present situation and forward prediction. Sci. Total. Environ., 693, 133557.
Spiegelhalter, D.J., Best, N.G., Carlin, B.P., Van Der Linde, A., 2002. Bayesian measures of model complexity and fit. Journal of the royal statistical society: Series b (statistical methodology), 64, 583-639.
Steger, S., Brenning, A., Bell, R., Petschko, H., Glade, T., 2016. Exploring discrepancies between quantitative validation results and the geomorphic plausibility of statistical landslide susceptibility maps. Geomorphology, 262, 8-23.
Steger, S. et al., 2021a. Correlation does not imply geomorphic causation in data-driven landslide susceptibility modelling–Benefits of exploring landslide data collection effects. Sci. Total.

Environ., 776, 145935.

Steger, S. et al., 2021b. Correlation does not imply geomorphic causation in data-driven landslide susceptibility modelling – Benefits of exploring landslide data collection effects. Sci. Total. Environ., 776, 145935.

Tanyaş, H., Görüm, T., Kirschbaum, D., Lombardo, L., 2022. Could road constructions be more hazardous than an earthquake in terms of mass movement? Nat. Hazards, 112, 639-663.

Tanyaş, H. et al., 2021. A closer look at factors governing landslide recovery time in post-seismic periods. Geomorphology, 391, 107912.

Tanyaş, H., Lombardo, L., 2019. Variation in landslide-affected area under the control of ground motion and topography. Eng. Geol., 260, 105229.

Titti, G., Napoli, G.N., Conoscenti, C., Lombardo, L., 2022a. Cloud-based interactive susceptibility modeling of natural hazards in Google Earth Engine.

Titti, G. et al., 2022b. Mapping Susceptibility With Open-Source Tools: A New Plugin for QGIS. Frontiers in Earth Science, 10.

Titti, G., van Westen, C., Borgatti, L., Pasuto, A., Lombardo, L., 2021. When Enough Is Really Enough? On the Minimum Number of Landslides to Build Reliable Susceptibility Models. Geosciences, 11, 469.

Tong, C. et al., 2017. Taiwan Climate Change Science Report. National Science and Technology Center for Disaster Reduction: Taipei, Taiwan.

Van den Bout, B., Lombardo, L., Chiyang, M., van Westen, C., Jetten, V., 2021. Physically-based catchment-scale prediction of slope failure volume and geometry. Eng. Geol., 284, 105942.

Van Westen, C., Rengers, N., Soeters, R., 2003. Use of geomorphological information in indirect landslide susceptibility assessment. Nat. Hazards, 30, 399-419.

Van Westen, C.J., Castellanos, E., Kuriakose, S.L., 2008. Spatial data for landslide susceptibility, hazard, and vulnerability assessment: an overview. Eng. Geol., 102, 112-131.

Verstappen, H.T., 1983. Applied geomorphology: geomorphological surveys for environmental development.

Wang, N. et al., 2022. Space-time susceptibility modeling of hydro-morphological processes at the Chinese national scale. Eng. Geol., 301, 106586.

Wang, N. et al., 2021. Using satellite rainfall products to assess the triggering conditions for hydro-morphological processes in different geomorphological settings in China. International Journal of Applied Earth Observation and Geoinformation, 102, 102350.

Wang, Y., Fang, Z., Hong, H., 2019. Comparison of convolutional neural networks for landslide susceptibility mapping in Yanshan County, China. Sci. Total. Environ., 666, 975-993.

Wei, L.W. et al., 2018. Adopting the I3–R24 rainfall index and landslide susceptibility for the establishment of an early warning model for rainfall-induced shallow landslides. Nat. Hazards Earth Syst. Sci., 18, 1717-1733.

Worden, C., Wald, D., 2016. ShakeMap manual online: technical manual, user's guide, and software guide. US Geol. Surv.

Wu, C.-H., 2015. Landslide susceptibility mapping by using landslide ratio-based logistic regression: A case study in the southern Taiwan. J. Mount. Sci, 12, 721-736.

Yang, W., Wang, Y., Sun, S., Wang, Y., Ma, C., 2019. Using Sentinel-2 time series to detect slope movement before the Jinsha River landslide. Landslides, 16, 1313-1324.

Youden, W.J., 1950. Index for rating diagnostic tests. Cancer, 3, 32-35.

Zevenbergen, L.W., Thorne, C.R., 1987. Quantitative analysis of land surface topography. Earth. Surf. Proc. Land, 12, 47-56.